Precision thermal control technology to enable thermally stable telescopes

Thomas E. Brooks and H. Philip Stahl*
NASA Marshall Space Flight Center, Huntsville, Alabama, United States

Abstract. The precision thermal control (PTC) project was a multiyear effort initiated in fiscal year 2017 to mature the technology readiness level (TRL) of technologies required to enable ultra-thermally stable ultraviolet/optical/infrared space telescope primary-mirror assemblies for ultra-high-contrast observations of exoplanets. PTC had three objectives: (1) validate thermal optical performance models, (2) derive thermal system stability specifications, and (3) demonstrate multi-zonal active thermal control. PTC successfully achieved its objectives and matured active thermal control technology to at least TRL-5. PTC's key accomplishments are a demonstration of better than 2-mK root-mean-square stable thermal control of the 1.5-m ultra-low-expansion (ULE®) Advanced Mirror Technology Development-2 (AMTD-2) mirror when exposed to thermal disturbances in a relevant thermal/vacuum environment, and the ability to shape the 1.5-m AMTD-2 mirror to picometer precision. Additionally, an analysis approach is demonstrated for quantifying thermally induced mid-spatial frequency error which can cause speckle noise in the coronagraph dark hole. [DOI: 10.1117/1.JATIS.8.2.024001]

Keywords: thermal control; space telescopes; astrophysics; astronomy; Habitable Exoplanet Observatory.

Paper 21137G received Oct. 27, 2021; accepted for publication Mar. 25, 2022; published online Apr. 22, 2022.

1 Introduction

"Are we alone?" is probably the most compelling question of our generation. According to the 2010 New Worlds, New Horizons decadal survey,[1] "one of the fastest growing and most exciting fields in astrophysics is the study of planets beyond our solar system. The ultimate goal is to image rocky planets that lie in the habitable zone of nearby stars." Directly imaging and characterizing habitable planets requires a large-aperture telescope with extreme wavefront stability. For an internal coronagraph, this requires correcting wavefront errors (WFEs) and keeping that correction stable to a few picometers (pm) root-mean-square (rms) for the duration of the science observation. This places severe constraints on the telescope and primary mirror (PM) performance. According to the 2015 Cosmic Origins Program Annual Technology Report,[2] a "thermally stable telescope" is critical, highly desirable technology for a strategic mission. "Wavefront stability is the most important technical capability that enables 10^{-10} contrast exoplanet science with an internal coronagraph. State of art for internal coronagraphy requires that the telescope must provide a wavefront that is stable at levels less than 10 pm for 10 minutes (stability period ranges from a few minutes to 10s of minutes depending on the brightness of the star being observed and the wavefront-sensing technology being used)."

To mature the technology needed for an exoplanet science thermally stable telescope by at least 0.5 technology readiness level (TRL), the precision thermal control (PTC) study defined three objectives to develop thermal design techniques validated by traceable characterization testing of components:

1. Validating models that predict optical performance of real mirrors and structure based on their structural designs and constituent material properties, i.e., coefficient of thermal expansion (CTE) distribution, thermal conductivity, thermal mass, etc.

---

*Address all correspondence to H. Philip Stahl, h.philip.stahl@nasa.gov

2. Deriving thermal system stability specifications from wavefront stability requirement.
3. Demonstrating the utility of a multi-zonal active thermal system for achieving control and stability.

To achieve its objectives, the PTC study defined a detailed technical plan with five quantifiable milestones:

1. Milestone 1: develop a high-fidelity model of the 1.5-m ultra-low-expansion (ULE®) Advanced Mirror Technology Development-2 (AMTD-2) mirror, including three-dimensional (3D) CTE distribution and reflective coating, that predicts its optical performance response to steady state and dynamic thermal gradients.
2. Milestone 2: derive specifications for thermal control system as a function of wavefront stability.
3. Milestone 3: design, build, and demonstrate a multi-zone thermal control system for a representative mirror assembly that senses temperature changes and actively controls the mirror's temperature.
4. Milestone 4: validate high-fidelity model by testing the 1.5-m ULE® AMTD-2 mirror in a relevant thermal vacuum environment at the Marshall Space Flight Center (MSFC) X-ray and Cryogenic Facility (XRCF) test facility.
5. Milestone 5: use a validated model to perform trade studies to optimize PM thermo-optical performance as a function of mirror design, material selection, material properties (i.e., CTE) mass, etc.

2 State of the Art

Thermal WFE occurs because of thermal expansion caused by the telescope's temperature changing when the telescope is slewed relative to the Sun. Thermal heat load changes cause the structure holding the mirrors to expand/contract, and the mirrors themselves to change shape. Fortunately, thermal drift tends to be slow, i.e., many minutes to hours. It is assumed that any drift that is longer than the wavefront sensing and control cycle will be corrected by a deformable mirror. Thus, the only concern is about stability errors that are shorter than 10 to 120 min. State of art (SOA) for ambient temperature space telescopes is "cold-biased" with heaters. The telescope is insulated from solar load such that, for all orientations relative to the Sun, if the heaters are off, it will always be below its set-point temperature. This ensures that the telescope's temperature is always under the control of heaters located on the forward straylight baffle tube as well as behind and beside the mirror.

No previous telescope has ever required picometer wavefront stability. The Hubble Space Telescope (HST) and the Webb Space Telescope (WST) illustrate the challenge. WST is in the shadow of its Sunshade in a thermally stable SE-L2 orbit. HST is in a heated tube in a thermally varying low-Earth orbit. When WST slews from its coldest to its warmest pointing, its temperature is predicted to change by 0.22 K, and its WFE is predicted to change by 31-nm rms. While not designed to do exoplanet science, it would take WST over 14 days to "passively" achieve the required level of stability for optical coronagraphy (Fig. 1).[3] Obviously, this is too long for exoplanet science. HST is a cold-biased telescope heated to an ambient temperature, but this environment is not controlled. The HST telescope's temperature changes by nearly 20°C as it orbits,[4] moving in and out of the Earth's shadow. This change causes the structure between the primary and secondary mirrors to change (typically $\pm 3\ \mu\text{m}$) resulting in WFE changes of 10 to 25 nm every 90 min (Fig. 2). Assuming linear performance, HST could be used for exoplanet science if its thermal variation were controlled to <20 mK. When a telescope, such as HST or WST slews or rolls relative to the Sun, the heat load onto the telescope's side and back changes—introducing axial and lateral gradients. These gradients cause the WFE to drift until the mirror reaches a new thermal equilibrium. The dominant WFE is power. The exact amplitude depends on the magnitude of the heat load change and the CTE of the mirror and structure.

To solve the focus problem, active thermal control was developed. The method with the most flight history is "bang–bang" control. Similar to a home thermostat, sensors are attached to the telescope, and if its temperature drops below a "set point," the heaters turn on. Once the temperature reaches another set point, they turn off (Fig. 3). The L3Harris Corporation NextView

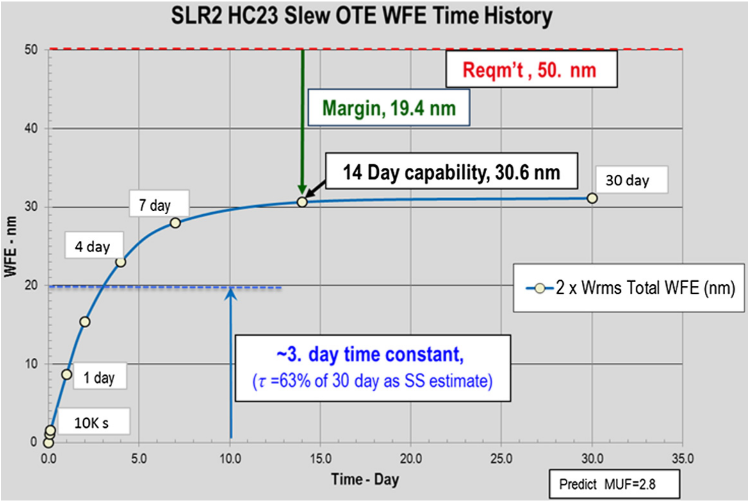

Fig. 1 Thermal modeling predicts that the passively cooled Webb Space Telescope's WFE changes by 31 nm over 14 days due to a worst-case thermal slew.[3]

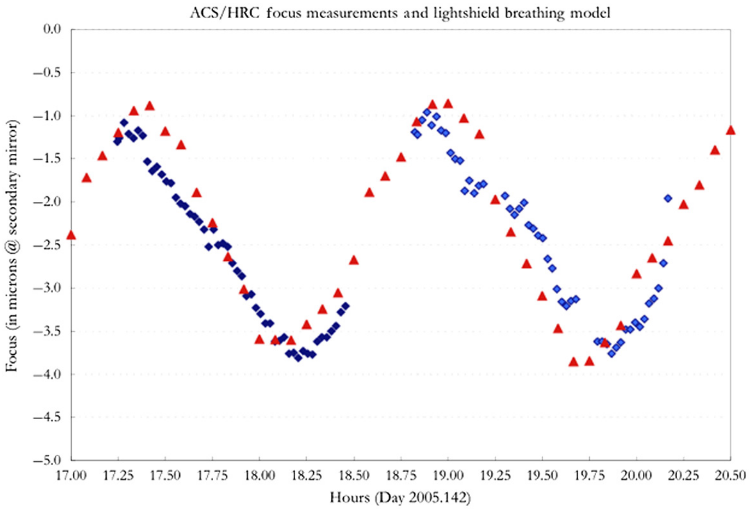

Fig. 2 The Hubble Space Telescope must be actively refocused as it goes in and out of the Earth's shadow resulting in WFE of up to 25 nms.[4]

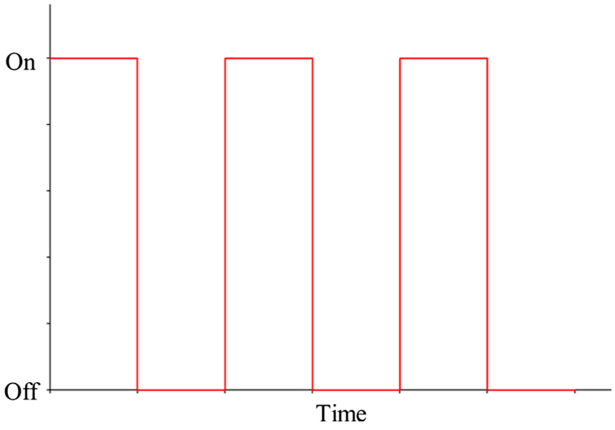

Fig. 3 Bang–bang control cycle.

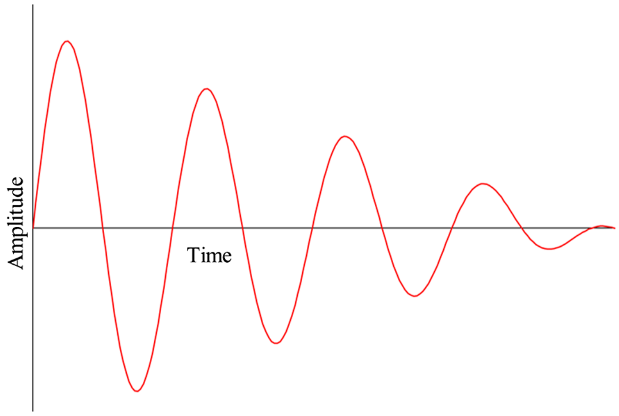

Fig. 4 Proportional control cycle.

telescope system has a bang–bang thermal control system. The NextView control system's deadband is ±300 mK, but the actual telescope temperature varies over a wider range (∼ ± 1 K). While sufficient for commercial imaging, it is insufficient for exoplanet science. An integrated model prepared for the Actively-Corrected Coronagraph for Exoplanet System Study (using a NextView telescope) predicted that after a 12-h settling time from a 30-deg rotation, the wavefront would have 151-pm rms of defocus and 19-pm rms of coma and astigmatism.[5]

Current SOA thermal control uses proportional integral derivative (PID) control (Fig. 4). PID control sets heater power levels equal to the sum of products of three tuning coefficients and a zone's temperature error (difference between set point and measurement), the derivative of the temperature error, and the integral of the temperature error. This method of control requires a power system capable of supplying proportional power. L3Harris Corporation has demonstrated TRL-9 proportional thermal control on their Spaceview™ telescopes. Their thermal control system's sensors have a noise of ∼50 mK and controls the 1.1-m telescope to a temperature stability of 100 to 200 mK.[6] PID control is a more complex and capable alternative to bang–bang. But both miss relevant, known information, such as when and how much the telescope slews, the power usage of telescope subsystems, and the temperatures of nearby components. As an example, in a proportional system, if one control zone is too hot while a nearby control zone is too cold, the cold control zone's heater will turn on and exacerbate the already too hot control zone's problem.

The solution is to place the PM inside a multi-zone thermal enclosure that can sense when and/or predict how the telescope's external thermal load changes (because of a slew or roll relative to the Sun) and modifies the amplitude of each zone's heater to compensate. Sensors measure the mirror's temperature distribution, estimate temperatures at unmeasured locations, and determine heating needed to produce the desired temperature profile. Based on a given slew or roll, the control system increases or decreases heater output in the appropriate zone to compensate. The goal is for the PM to see no temperature change, regardless of where the telescope points on the sky.

One approach that PTC investigated is model predictive control (MPC).[7,8] MPC places a physics-based model into the control loop to determine control variables (heater power levels) based on state variables (temperature measurements). MPC determines heater power levels using a different logic than proportional control. Proportional control adjusts heater power in proportion to the difference between measured and desired temperatures at a single location following an equation:

$$Q_i = K_p * (T_{d,i} - T_{m,i}), \tag{1}$$

where K_p is the proportional gain coefficient, $T_{d,i}$ is the desired temperature at control zone i, and $T_{m,i}$ is the measured temperature at control zone i. MPC uses multiple control zones. MPC starts with a system of equations based on the physics (including radiation, telescope slews, and other environment effects) governing a control case. Then, to achieve control, uses a numerical version of the heat equation to back solve for the heat distribution that gives the desired temperature distribution where C_i is the heat capacitance of volume i, Δt is the timestep, T is the temperature at the timestep denoted in the superscript and the volume denoted in the subscript, Q_i is the heating internal to volume i (heater power in a control system), G is a linear conductor between the volumes denoted in its subscript, and $\hat{G}$ is a radiative conductor between the volumes denoted in its subscript

$$2\frac{C_i}{\Delta t}(T_i^{n+1} - T_i^n) = 2Q_i + Q^n + Q^{n+1}, \tag{2}$$

$$Q^n = \sum_{j=1}^{N}[G_{ji}(T_j^n - T_i^n) + \hat{G}_{ji}\{(T_j^n)^4 - (T_i^n)^4\}], \tag{3}$$

$$Q^{n+1} = \sum_{j=1}^{N}[G_{ji}(T_j^{n+1} - T_i^{n+1}) + \hat{G}_{ji}\{(T_j^{n+1})^4 - (T_i^{n+1})^4\}]. \tag{4}$$

MPC takes into account the interdependency between all of the control zone's temperatures and commands such that all of the zonal heaters work as a collective.

One problem with MPC is that it is computationally expensive and may not be appropriate for systems that require thermal control on the order of a few seconds. And, it requires a high-fidelity "as-built" model. Artificial intelligence (AI) control may be better than MPC. The universal approximation theorem states that a feed-forward network constructed of artificial neurons can approximate any continuous function,[9] i.e., it does not need an as-built model. And, it has significantly faster execution time. Therefore, it seems likely that such a network can approximate the interaction between all known state variables and the heater power.

Over the course of this study, all three approaches (PID, MPC, and AI) were evaluated via benchtop testing. The PID controller performed best. The best MPC control system was too slow, and the best AI system was not reliably intelligent, and therefore, had poor performance. We can note that this result does not preclude the possibility that future development may improve AI or MPC thermal control from being useful for a flight program.

3 Accomplishments

3.1 *Objective 1: Validate High-Fidelity Structural-Thermal-Optical-Performance Model*

Designing a telescope to have an ultra-stable wavefront requires using a validated high-fidelity structural-thermal-optical-performance (STOP) model to predict thermal optical performance of mirrors and structure based on their mechanical designs and material properties, i.e., CTE distribution, thermal conductivity, thermal mass, etc.

3.1.1 *Milestone 1: develop a high-fidelity STOP model of the 1.5-m ULE® AMTD-2 mirror*

A high-fidelity STOP model of the AMTD-2 1.5-m ULE® mirror was created in NASTRAN that accurately models its as-built mechanical dimensions and CTE distribution.[10–13] The as-built mechanical dimensions were quantified using 3D x-ray computed tomography (CT) to measure the internal structure of the mirror (Fig. 5). A custom algorithm was written to convert the x-ray CT 3D mapping into a finite element model. To add a 3D mapping of CTE distribution to the STOP model, Harris Corporation provided MSFC with Corning CTE data maps for each of the 18 core elements and the location of each element in the core (Fig. 6).

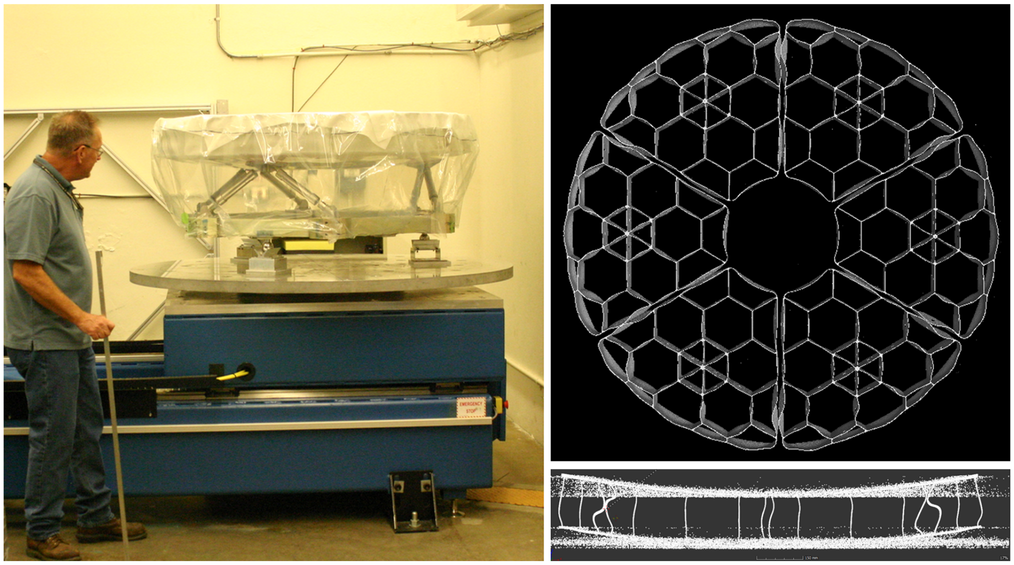

(a) (b)

Fig. 5 (a) 1.5-m AMTD-2 mirror was placed in MSFC's x-ray computer tomography test setup and (b) its internal structure quantified.

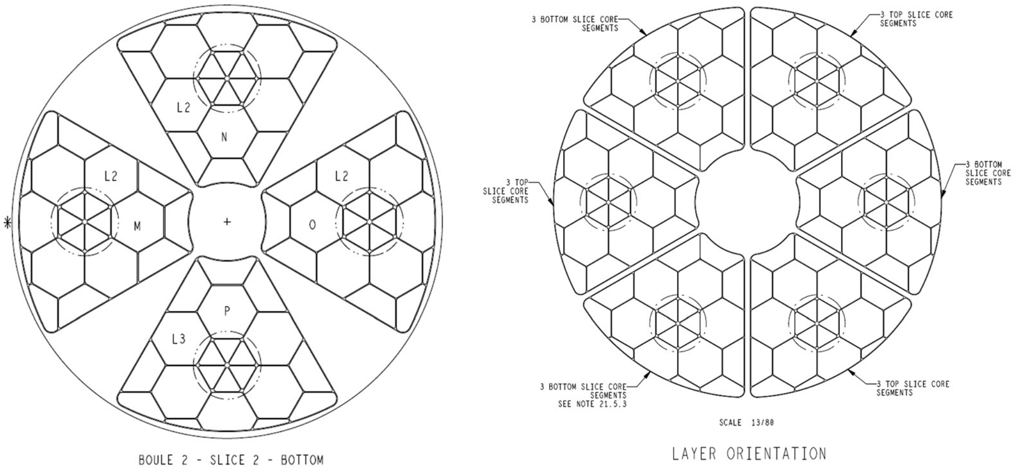

(a) (b)

Fig. 6 (a) L3Harris Corp. provided Corning CTE data of where each core element was cut from its boule and (b) the location of that core element in the AMTD-2 mirror.

3.1.2 *Milestone 4: validate high-fidelity STOP model by testing the 1.5-m ULE® AMTD-2 mirror in a relevant thermal vacuum environment at the MSFC XRCF test facility*

The high-fidelity STOP model was validated by correlating its predictions with interferometric measurement of the mirror's surface figure response in a 231-K static thermal soak test and to an 87.7-K thermal gradient test. The soak test was performed by cooling the mirror to 231 K and, after stabilized, its surface figure was measured and subtracted from its starting temperature shape to quantify its cryo-deformation. To quantify linearity, measurements are taken at multiple set points between 230 K and ambient. The gradient test was performed by placing the mirror in an ambient vacuum environment and illuminating its side with an array of solar lamps. To enable STOP modeling, the mirror was fully instrumented with thermal sensors to provide knowledge of its temperature distribution (Fig. 7). Both tests were conducted as part of the final AMTD-2 thermal test.[11–14]

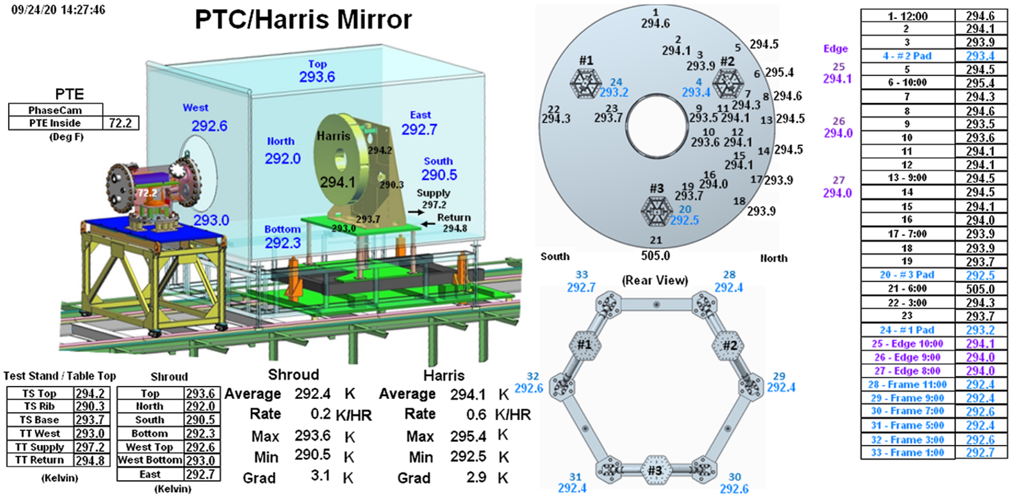

Test Stand / Table Top	(Kelvin)
TS Top	294.2
TS Rib	290.3
TS Base	293.7
TT West	293.0
TT Supply	297.2
TT Return	294.8

Shroud	(Kelvin)
Top	293.6
North	292.0
South	290.5
Bottom	292.3
West Top	292.6
West Bottom	293.0
East	292.7

Shroud		
Average	292.4	K
Rate	0.2	K/HR
Max	293.6	K
Min	290.5	K
Grad	3.1	K

Harris		
Average	294.1	K
Rate	0.6	K/HR
Max	295.4	K
Min	292.5	K
Grad	2.9	K

1- 12:00	294.6
2	294.1
3	293.9
4 - #2 Pad	293.4
5	294.5
6 - 10:00	295.4
7	294.3
8	294.6
9	293.5
10	293.6
11	294.1
12	294.1
13 - 9:00	294.5
14	294.5
15	294.1
16	294.0
17 - 7:00	293.9
18	293.9
19	293.7
20 - #3 Pad	292.5
21 - 6:00	505.0
22 - 3:00	294.3
23	293.7
24 - #1 Pad	293.2
25 - Edge 10:00	294.1
26 - Edge 9:00	294.0
27 - Edge 8:00	294.0
28 - Frame 11:00	292.4
29 - Frame 9:00	292.4
30 - Frame 7:00	292.6
31 - Frame 5:00	292.4
32 - Frame 3:00	292.6
33 - Frame 1:00	292.7

Fig. 7 PTC test setup. Mirror fully instrumented with thermal sensors in cryo-shroud.

The STOP model's performance prediction is composed of two parts: (1) the opto-mechanical-thermal deformation of the mirror mount system and (2) the mirror substrate's CTE distribution (Fig. 8). Each component was correlated with the test data separately to minimize the residual error. First, the mount effect deformation is removed, then the CTE distribution deformation. As the temperature of the mirror and mount changes from 293 to 231 K, the aluminum backplane contracts, and the mount struts apply a prying force to the mirror. Even though the design is symmetric, the prying signature is not, which means that the as-built mount has unintended asymmetries. The STOP model applies a combination of inferred prying forces to the bond pad that most closely match the test data. Based on the mirror's measured temperature deformation, the STOP model predicts a mount distortion of 18.9-nm rms and a CTE inhomogeneity distortion of 16.6-nm rms resulting in a total cryo-deformation of 24.7-nm rms (Fig. 8). After subtracting mount and CTE effects, the high-fidelity model has a residual error of 13.4-nm rms (Fig. 9).[14]

To further validate the high-fidelity model, the 1.5-m ULE® AMTD-2 mirror's response to a lateral thermal gradient was characterized. The mirror was placed in the XRCF under ambient vacuum and illuminated, to create a thermal gradient, by a solar lamp. This was a bare-mirror-only test, i.e., mirror only with no thermal control system (Fig. 10). Based on thermocouple data on back of mirror, thermal desktop calculated a $\Delta T = 87.7$-K peak-to-valley (PV) temperature distribution (hot side ∼100°C and cold side ∼20°C) for when the heat lamps operated at 406 W. The measured surface deformation for this thermal gradient was 78.6-nm rms.

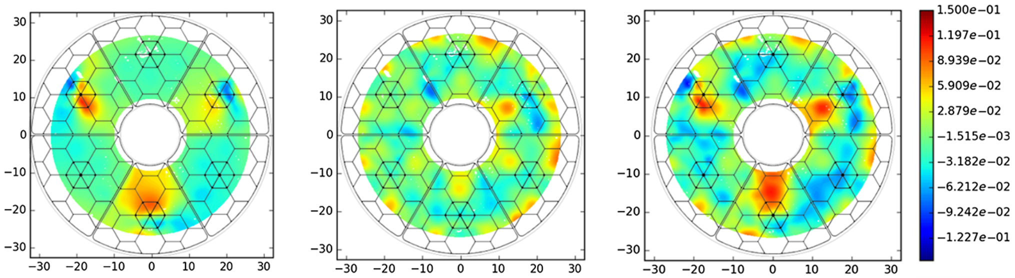

Mount Effects 18.9 nm rms + CTE Inhomogeneity 16.6 nm RMS = Predicted Deformation 24.7 nm RMS

Fig. 8 STOP model predicted 24.7-nm rms total cryo-deformation consists of 18.9 nm rms caused by mount effects and 16.6-nm rms caused by CTE inhomogeneity. (All plots have same vertical scale.)

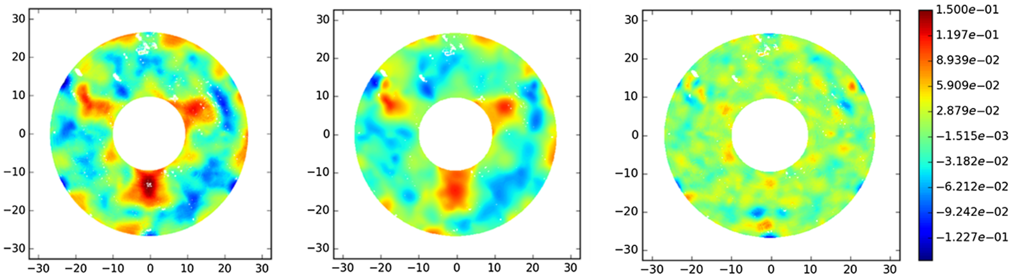

Measured
28.8 nm rms
-
Predicted
24.7 nm RMS
=
Residual
13.4 nm RMS

Fig. 9 STOP Model was correlated with measured data to minimize residual error. (All plots have the same vertical scale.)

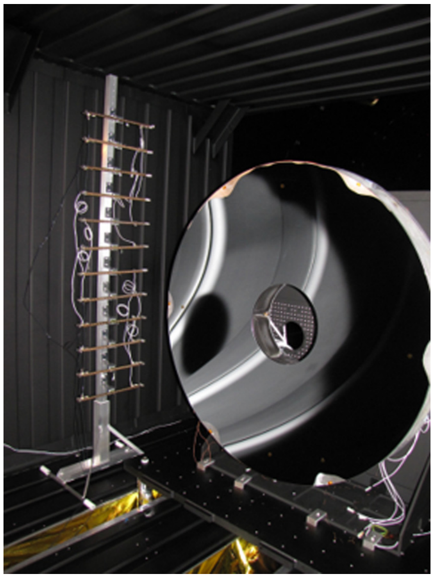

Fig. 10 1.5-m AMTD-2 ULE® mirror tested inside XRCF cryo-shroud at ambient vacuum with a single lamp array to impose lateral thermal gradient.

To match the measured figure change (with a correlation error of 38 nm rms), the STOP model increased the average substrate CTE to 81 ppb/K[11] (Fig. 11). The magnitude of the CTE increase is consistent with Corning-published data that ULE® bulk CTE changes from ≈0 ppb/K at 20°C to ≈80 ppb/K at 100°C (Fig. 12).[15] The correlation error would have been smaller if the model had applied a CTE gradient corresponding to the local temperature instead of a bulk change.

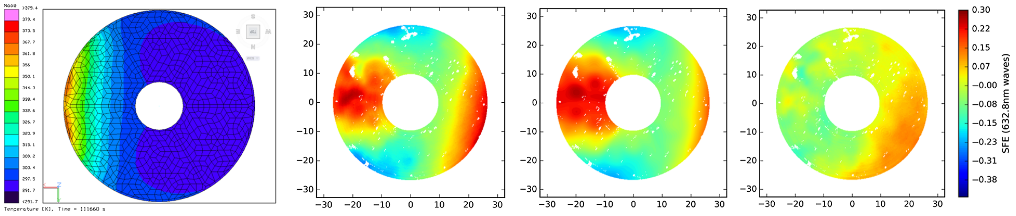

87.7 K thermal gradient
78.6 nm measured
Model correlation
38 nm rms correlation error

Fig. 11 Thermal gradient ($\Delta T = 87.7$ KPV) resulted in a measured surface figure change of 78.6 nm rms. To match measured change, STOP model increased average substrate CTE to 81 ppb/K.[11] Model correlation Error is 38-nm rms. (All surface plots have the same vertical scale.)

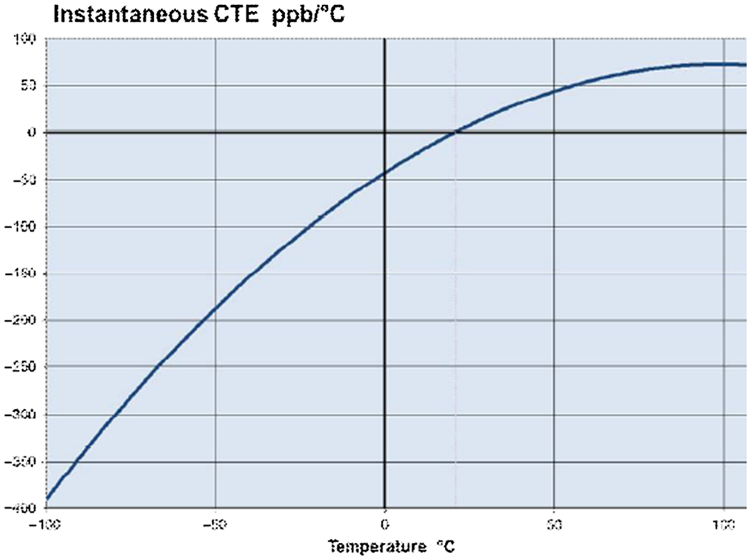

Fig. 12 Corning ULE® bulk CTE increases from ≈0 ppb/K at 20°C to ≈75 to 80 ppb/K at 100°C.[15]

3.2 *Objective 2: Derive Traceable Specifications for an Active Thermal Control System*

Designing a telescope to have an ultra-stable wavefront via active thermal control requires a validated STOP model to help define the thermal control system's specifications, such as: sensing resolution (1 or 10 or 50 mK), control accuracy (10 or 50 mK), control period (1 or 5 or 20 min), number and distribution of sense and control zones.[8]

3.2.1 *Milestone 2: derive specifications for thermal control system as a function of wavefront stability*

Analysis conducted as part of the AMTD study indicated that exo-Earth science with a coronagraph requires a wavefront stability of 10-pm per 10-min.[13,16,17] Thermal modulation transfer function (MTF) modeling[7,8,13] provided an analytical tool for designing a telescope to have this level of thermal stability. Thermal MTF analysis decomposes the telescope's thermal environment into a set of periodic thermal oscillations and calculated the resulting WFE caused by each oscillation (Fig. 13). Consistent with expectation, the magnitude of the WFE response depends linearly on the amplitude and period of the input thermal oscillation and the telescope's thermal time constant, determined by the telescope's thermal properties (i.e., mass and conductivity).

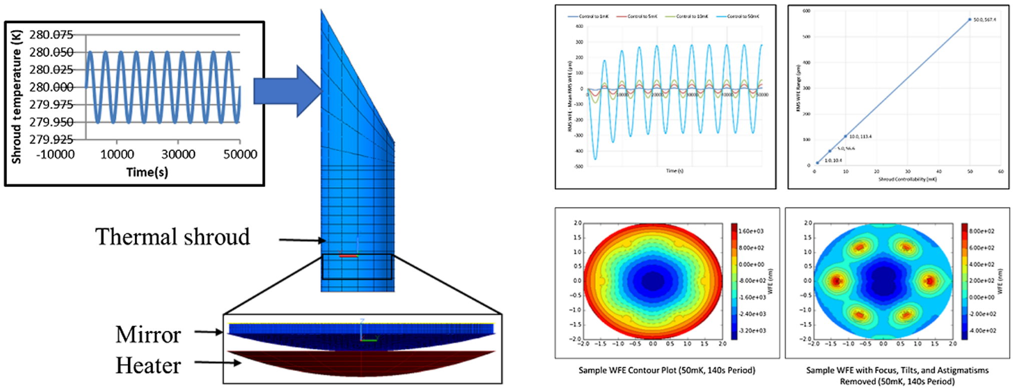

Fig. 13 Thermal control period to achieve a given WFE stability is inversely proportional to thermal controllability noise and thermal sensitivity. WFE stability tolerance can be achieved by a range of sensor noise uncertainty and control period.[13]

Integrated modeling shows that WFE stability is inversely proportional to the mirror's mass and specific heat, and linearly proportional to the mirror's CTE,[13] and the thermal control system's controllability fluctuation (i.e., noise) and control period.

Given that the analysis indicates that thermal performance is linear, picometer wavefront stability can be achieved by either controlling the shroud to a small temperature (10 mK) or by rapidly correcting the temperature (Fig. 14). Additional stability can be achieved by increasing the system's thermal mass. This is particularly relevant to potential telescopes, such as Habitable Exoplanet Observatory (HabEx), which might have large monolithic PMs. Thus, as long as one senses faster than the mirror's thermal response time, there are a range of control solutions; and the faster the control cycle, the less precise the sensing needs to be.

The purpose of Objective 2 was to expand upon that initial AMTD study and derive a specification for a real telescope. Originally, Milestone 2 was intended to inform Milestone 5, but it was quickly determined that, because of the feedback loop between the PM design and the thermal enclosure specification, they had to be done together. As a result, a 1.1-mK-rms thermal stability specification was defined for the HabEx baseline PM thermal control system. And a multi-zone thermal system was designed to achieve this specification with 86 control zones on the PM and its hexapods, thermal sensors with 50-mK measurement uncertainty, and proportional controller (PID) systems operating with 30-s periods.[18–20]

Deriving a specification for a potential HabEx PM active control system required three steps: (1) defining an error budget, (2) defining the baseline PM's thermal sensitivity by creating a thermal model of the telescope, and (3) exercising the thermal model for multiple (including one final) design reference missions (DRMs).[12]

A Zernike polynomial-based wavefront stability error budget was derived from the total maximum allowed vector vortex coronagraph (VVC) leakage to detect an exo-Earth.[21,22] The process starts by calculating the amount of raw contrast leakage that a coronagraph can have and still detect an exo-Earth relative to its host star, at a signal-to-noise ratio of 7. For the case illustrated in Fig. 15, this is 40-parts-per-trillion (regardless of where the exo-Earth is located in the dark hole). Next, the contrast leakage sensitivity of the coronagraph is calculated for each Zernike polynomial. Finally, the allowed 40-ppt contrast leakage is allocated across all Zernike polynomials and converted into WFE. For example, the vector vortex charge 4 coronagraph (VVC-4) is insensitive to tilt and power; therefore, more error can be allocated to these terms, but all higher-order terms must be very stable. As shown in Fig. 16, the error budget can

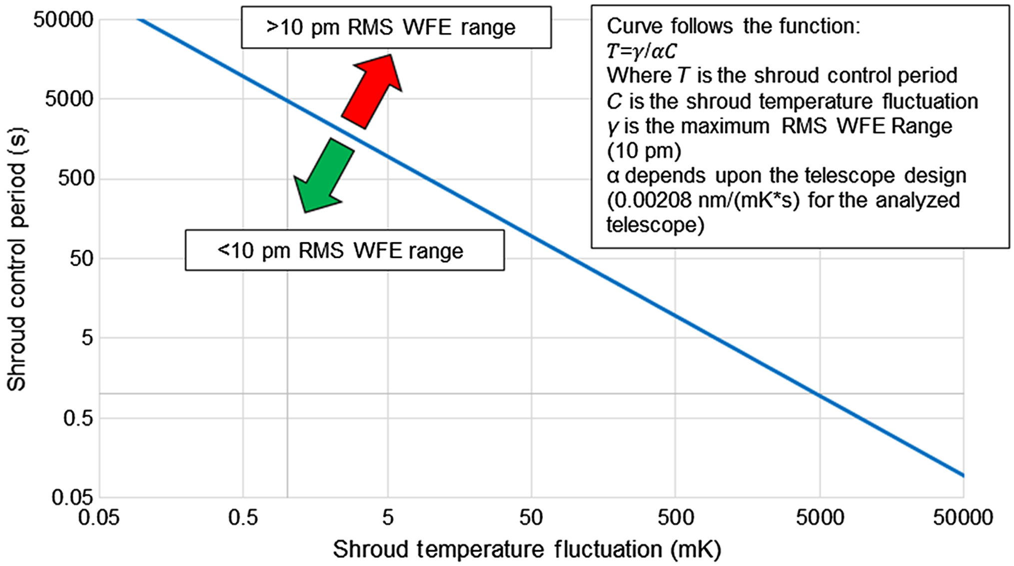

Fig. 14 (a) WFE versus shroud thermal control amplitude for 5000-s control period. (b) WFE versus shroud control period for 50-mK control amplitude. (c) WFE versus mirror mass and shroud control amplitude for 140-s control period. (d) WFE stability tolerance can be achieved by a range of sensor noise uncertainty and control period.[7,8]

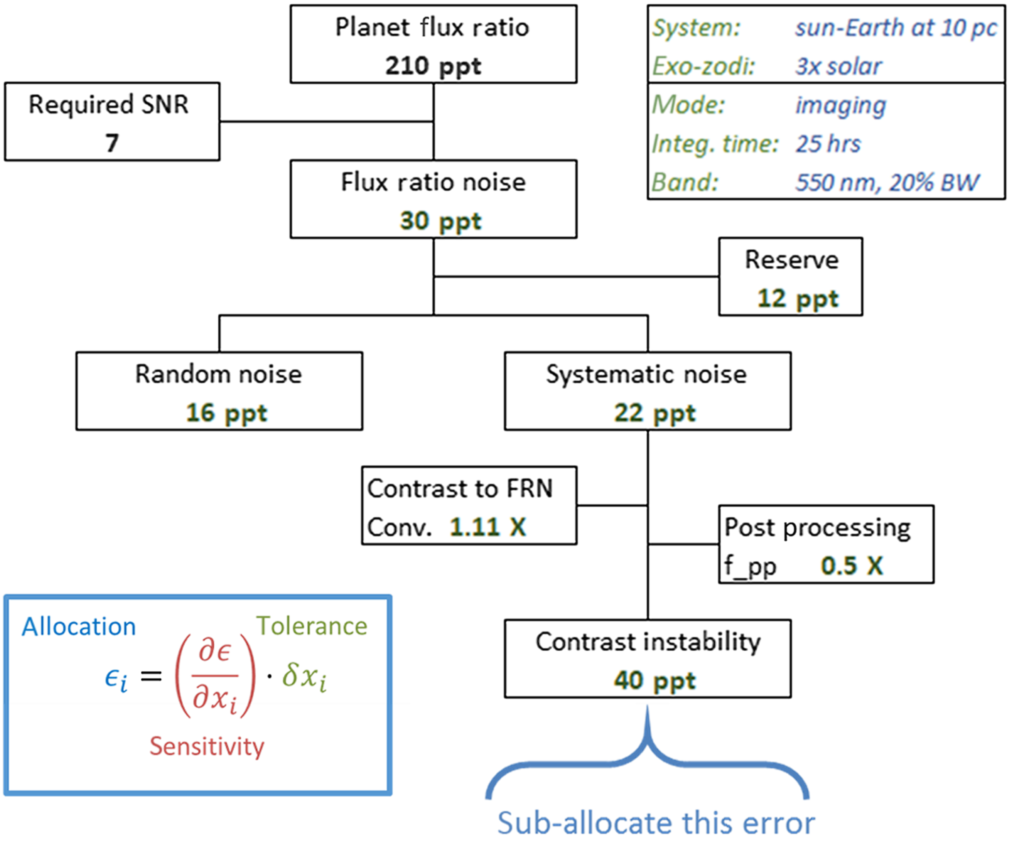

Fig. 15 Wavefront stability error budget development method.[21,22]

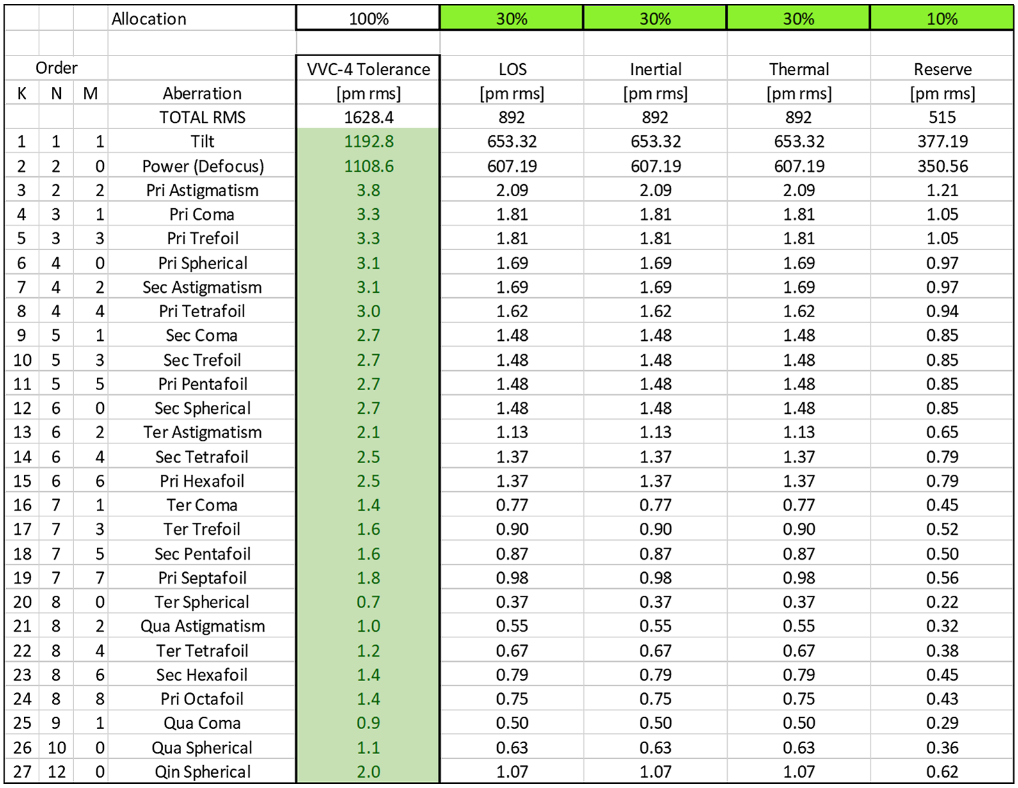

			Allocation	100%	30%	30%	30%	10%
Order				VVC-4 Tolerance	LOS	Inertial	Thermal	Reserve
K	N	M	Aberration	[pm rms]	[pm rms]	[pm rms]	[pm rms]	[pm rms]
			TOTAL RMS	1628.4	892	892	892	515
1	1	1	Tilt	1192.8	653.32	653.32	653.32	377.19
2	2	0	Power (Defocus)	1108.6	607.19	607.19	607.19	350.56
3	2	2	Pri Astigmatism	3.8	2.09	2.09	2.09	1.21
4	3	1	Pri Coma	3.3	1.81	1.81	1.81	1.05
5	3	3	Pri Trefoil	3.3	1.81	1.81	1.81	1.05
6	4	0	Pri Spherical	3.1	1.69	1.69	1.69	0.97
7	4	2	Sec Astigmatism	3.1	1.69	1.69	1.69	0.97
8	4	4	Pri Tetrafoil	3.0	1.62	1.62	1.62	0.94
9	5	1	Sec Coma	2.7	1.48	1.48	1.48	0.85
10	5	3	Sec Trefoil	2.7	1.48	1.48	1.48	0.85
11	5	5	Pri Pentafoil	2.7	1.48	1.48	1.48	0.85
12	6	0	Sec Spherical	2.7	1.48	1.48	1.48	0.85
13	6	2	Ter Astigmatism	2.1	1.13	1.13	1.13	0.65
14	6	4	Sec Tetrafoil	2.5	1.37	1.37	1.37	0.79
15	6	6	Pri Hexafoil	2.5	1.37	1.37	1.37	0.79
16	7	1	Ter Coma	1.4	0.77	0.77	0.77	0.45
17	7	3	Ter Trefoil	1.6	0.90	0.90	0.90	0.52
18	7	5	Sec Pentafoil	1.6	0.87	0.87	0.87	0.50
19	7	7	Pri Septafoil	1.8	0.98	0.98	0.98	0.56
20	8	0	Ter Spherical	0.7	0.37	0.37	0.37	0.22
21	8	2	Qua Astigmatism	1.0	0.55	0.55	0.55	0.32
22	8	4	Ter Tetrafoil	1.2	0.67	0.67	0.67	0.38
23	8	6	Sec Hexafoil	1.4	0.79	0.79	0.79	0.45
24	8	8	Pri Octafoil	1.4	0.75	0.75	0.75	0.43
25	9	1	Qua Coma	0.9	0.50	0.50	0.50	0.29
26	10	0	Qua Spherical	1.1	0.63	0.63	0.63	0.36
27	12	0	Qin Spherical	2.0	1.07	1.07	1.07	0.62

Fig. 16 Allocation of WFE stability between LOS, inertial and thermal sources.[12]

be further sub-allocated between thermal, inertial, and line-of-sight (LOS) WFE. References 18–20 provide a VVC-6 error budget and STOP model analysis for the baseline HabEx telescope.

Next, an integrated observatory thermal model was created in thermal desktop using a geometry created in pro-engineer CAD.[12,19,20] The thermal desktop model has 20,000 elements and calculates telescope's structure and mirror temperature distribution at 10,000 nodes. The temperature distribution for each node is mapped onto the NASTRAN finite element model, and the deflections created by each node's CTE is calculated using NASTRAN Solution 101. Rigid body motions and mirror surface deformations are calculated from the NASTRAN deflections using SigFit. The primary and secondary mirror's mesh grids were sized to enable SigFit to fit thermally induced surface figure error (SFE) to higher-order Zernike polynomials.

The model assumes multi-layer insulation (MLI) to control heat loss and to isolate thermal disturbances (i.e., the Sun). Radiators pull heat from the science instruments and spacecraft electronics. Because of the MLI and radiators, the payload is passively cold-biased, and active thermal control is required to maintain the PM at an operating temperature of ∼270 K. Without heaters, the model predicts a PM temperature of 206 K. The model assumes TRL-9 components for the PM thermal enclosure: sensors with 50-mK measurement uncertainty, and proportional controller systems (PID) operating with 30-s periods. The model has 86 control zones on the PM and its hexapods. The model predicts that the PM front surface will have ∼200-mK "trefoil" thermal gradient (Fig. 17). The source of this gradient is thermal conduction into the hexapod struts. And, the model predicts that the mirror will have ∼3-K front to back gradient.

The primary and secondary mirror CTE is modeled as consisting of a uniform "bulk" CTE and a CTE homogeneity distribution. The uniform CTE value determines the mirror's low-order shape response to bulk temperature changes, and/or gradient temperature changes (i.e., axial, radial, or lateral). Such temperature changes can produce low-order errors such as power and astigmatism. The homogeneity distribution determines the mirror's mid-spatial response. The model calculates mirror shape changes from two effects: (1) response of mirror with uniform CTE to changes in temperature at each of the 10,000 nodes, and (2) response of a mirror with a CTE inhomogeneity distribution to a uniform bulk temperature change. One method to estimate CTE inhomogeneity is to measure the thermal deformation of the mirror and assume that CTE is linear with temperature. As part of the AMTD project, a 1.2-m Extremely Lightweight Zerodur® Mirror (ELZM) was measured to have an ∼11-nm-rms deformation over a 62-K thermal range (from 292 to 230 K). Figure 18 shows the measured error and its decomposition into Zernike polynomials.[23] The model assumes this measured thermal signature for its CTE inhomogeneity distribution.

The model was used to predict thermal performance for a potential science DRM. The DRM starts by pointing the telescope at a reference star to dig the dark hole in the coronagraph.

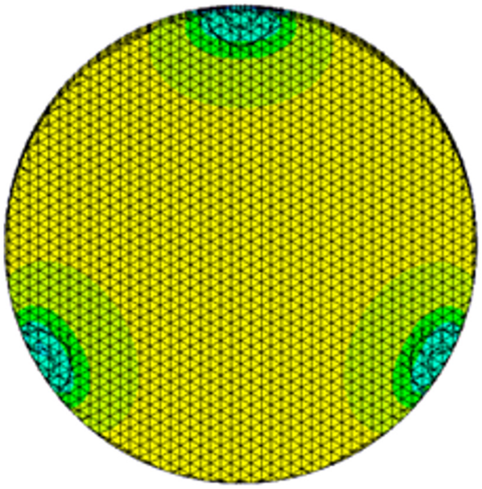

Fig. 17 Predicted 200-mK trefoil thermal distribution of PM front surface.

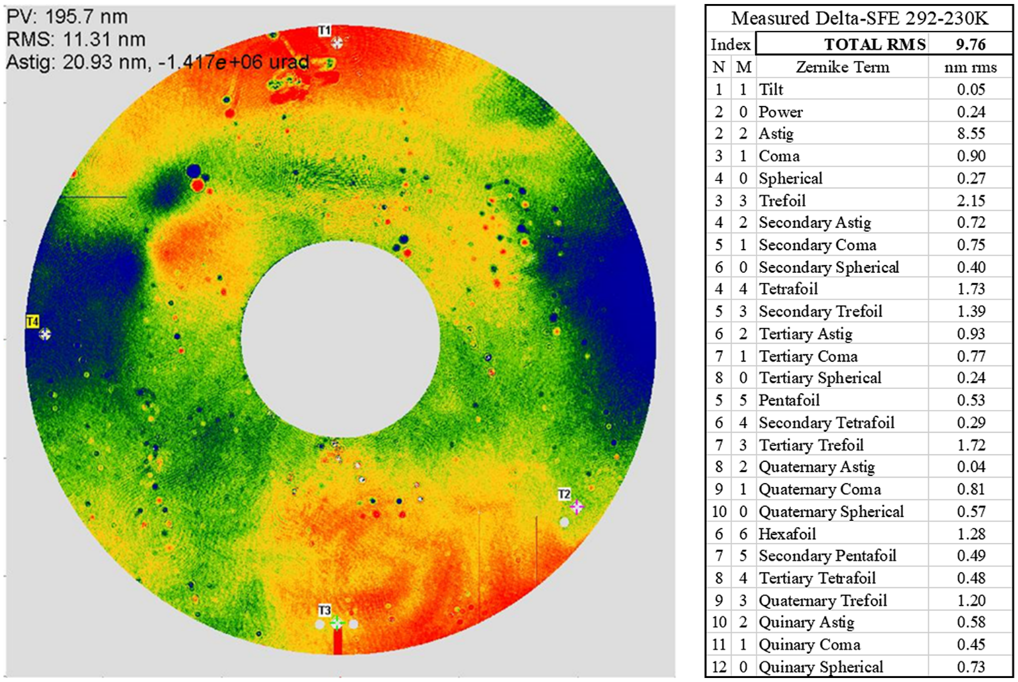

Measured Delta-SFE 292-230K

N	M	Zernike Term	nm rms
Index		TOTAL RMS	9.76
1	1	Tilt	0.05
2	0	Power	0.24
2	2	Astig	8.55
3	1	Coma	0.90
4	0	Spherical	0.27
3	3	Trefoil	2.15
4	2	Secondary Astig	0.72
5	1	Secondary Coma	0.75
6	0	Secondary Spherical	0.40
4	4	Tetrafoil	1.73
5	3	Secondary Trefoil	1.39
6	2	Tertiary Astig	0.93
7	1	Tertiary Coma	0.77
8	0	Tertiary Spherical	0.24
5	5	Pentafoil	0.53
6	4	Secondary Tetrafoil	0.29
7	3	Tertiary Trefoil	1.72
8	2	Quaternary Astig	0.04
9	1	Quaternary Coma	0.81
10	0	Quaternary Spherical	0.57
6	6	Hexafoil	1.28
7	5	Secondary Pentafoil	0.49
8	4	Tertiary Tetrafoil	0.48
9	3	Quaternary Trefoil	1.20
10	2	Quinary Astig	0.58
11	1	Quinary Coma	0.45
12	0	Quinary Spherical	0.73

Fig. 18 1.2-m Schott ELZM 62K thermal deformation decomposed into Zernikes.[23]

The analysis assumes that the telescope reaches a steady-state thermal condition at this Sun orientation. Next, the telescope is pointed at the science star. To make the analysis "worst-case," it is assumed that when the telescope is pointing at the reference star, the Sun is perpendicular to the Sunshade/solar panels with a 0-deg roll. And, when it points at the science star, it pitches away from the Sun (Fig. 19). Figure 20 shows the DRM motions as viewed from the Sun.

Figures 21–23 show how well the modeled active zonal thermal enclosure controls the temperature of the PM for a DRM consisting a 75-deg pitch of the telescope after it has spent 20 h pointing at a reference star to dig the dark hole followed by a 30-deg roll (from +15 deg to –15 deg) at 45 h. Figure 21 shows the predicted change in average bulk temperature and axial gradient temperature of the PM if there were no active control. It is noteworthy that the axial gradient changes faster than the average temperature; this will have WFE impact. Figures 22 and 23 show the predicted average and gradient temperature changes for the PM under active thermal control. The zonal control system keeps the PM average bulk temperature change to $<\sim 0.035$ mK and the axial gradient change to $<\sim 1.75$ mK.

To calculate PM wavefront stability, thermal desktop calculated its temperature distribution as a function of time, and NASTRAN calculated the surface deformations produced by

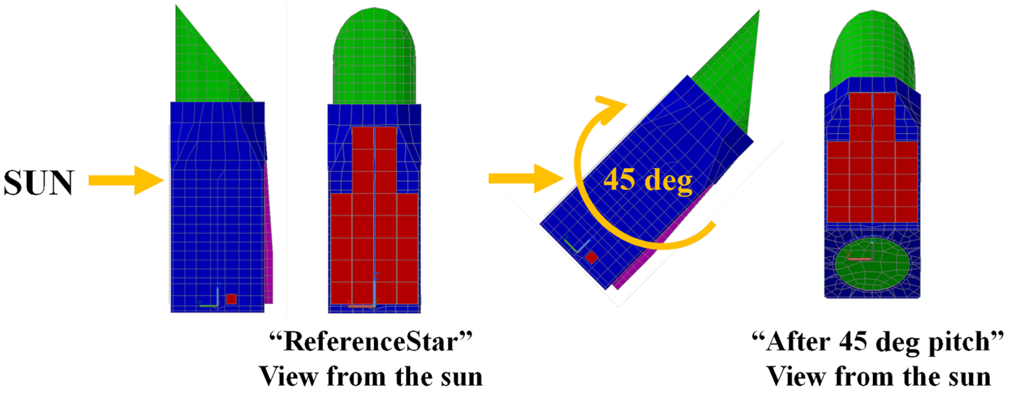

Fig. 19 Nominal observing scenario slews for thermal analysis.

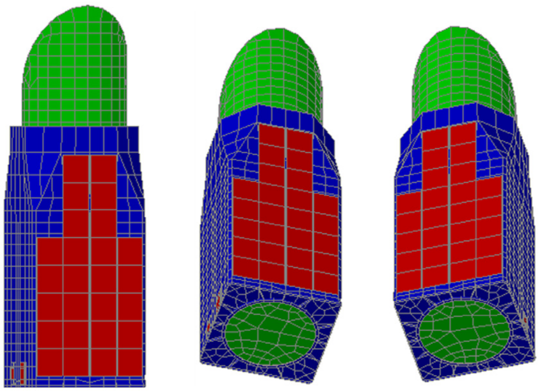

Fig. 20 Telescope motions as viewed from the Sun.

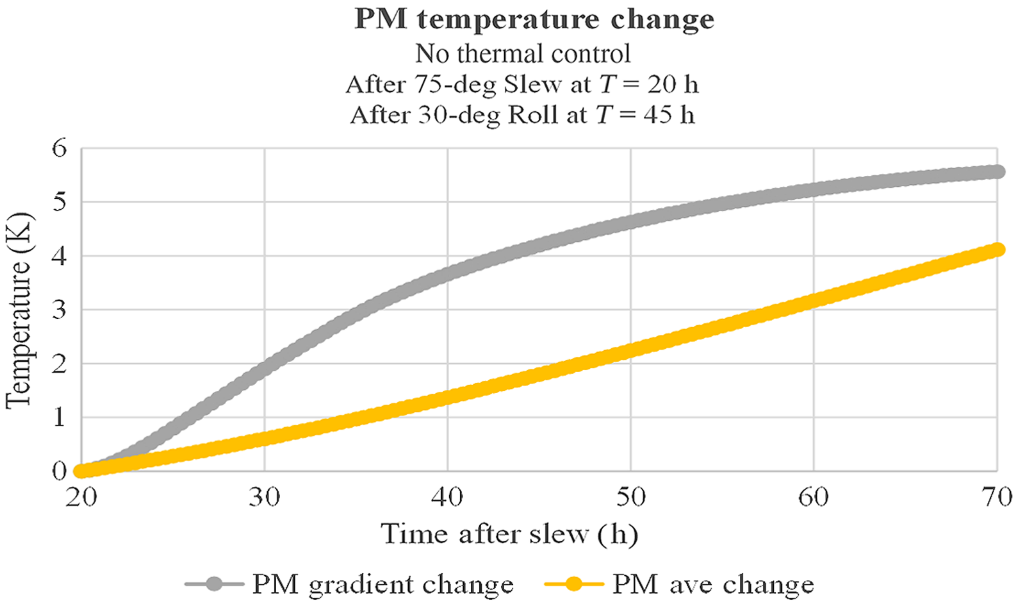

Fig. 21 Passive PM average and axial gradient temperature change from 75-deg pitch.

that distribution. The temporal WFE was then decomposed into Zernike polynomials by SigFit. Figure 24 shows the change in PM WFE produced by the 75-deg thermal slew DRM with no active thermal control. Figure 25 shows the change in the PM WFE caused by the 75-deg slew DRM with active zonal thermal control. Because the control system is able to keep the average and axial gradient temperatures very small, the thermal WFE remains <1-pm rms. As shown in Fig. 26, the predicted PM thermal WFE stability has significant performance margin relative to the error budget tolerance. The most important errors are astigmatism and coma.

3.2.2 *Milestone 5: use validated model to perform trade studies to optimize primary mirror thermo-optical performance as a function of mirror design, material selection, material properties (i.e., CTE) mass, etc.*

PTC, in conjunction with the HabEx study, performed multiple trade studies with literally hundreds of variations to optimize the primary mirror's stiffness, mass, gravity sag, and thermo-optical performance.[24] The baseline HabEx PM design was selected based on its predicted thermo-optical performance.[19,20,24]

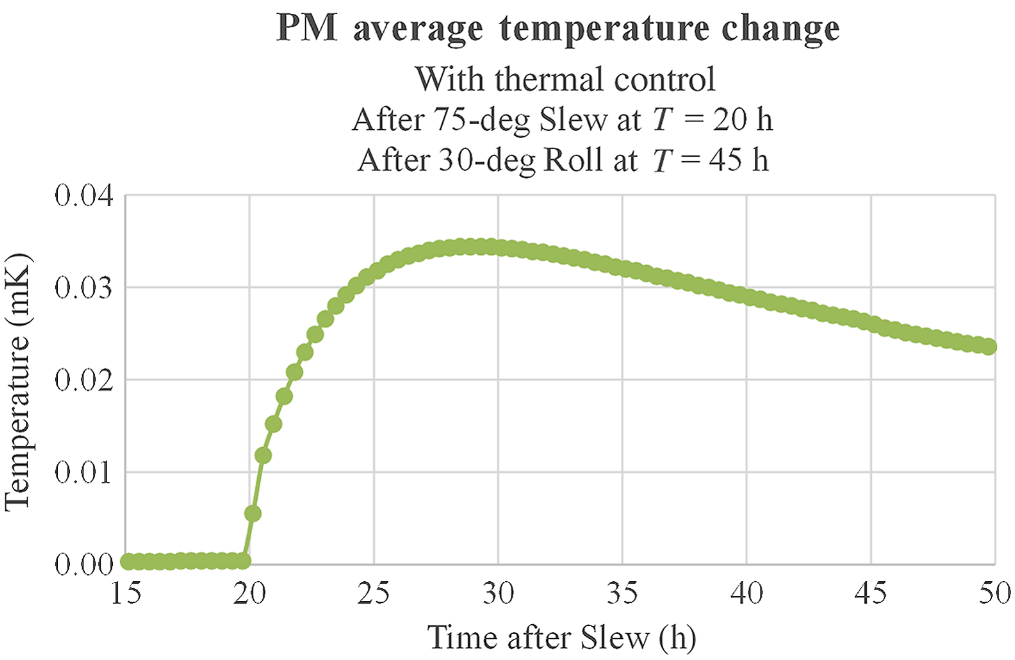

Fig. 22 Actively controlled PM average bulk temperature change from 75-deg pitch.

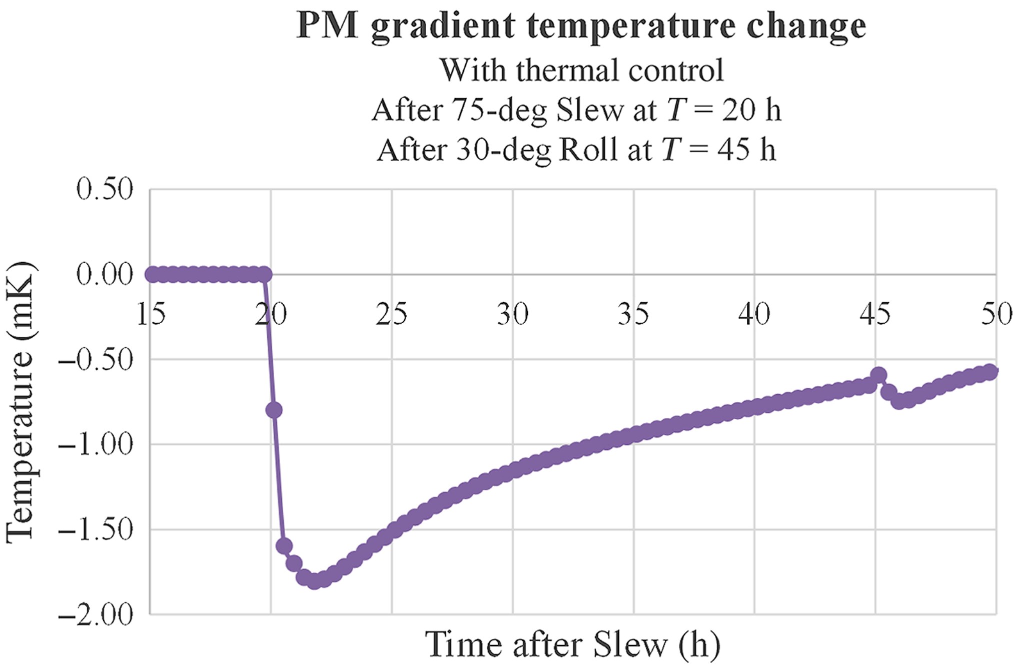

Fig. 23 Actively controlled PM axial temperature gradient change from 75-deg pitch.

Both Zerodur® and ULE® designs were considered. Both materials are TRL-9 with multiple mirrors currently flying in space. Both Schott and Corning can tailor their respective material's zero CTE temperature, and both claim similar CTE homogeneity (i.e., ∼5 ppb/K).[15,25] Therefore, a mirror manufactured from either material should have similar thermal performance. But the real impact of this design decision is architectural—whether the mirror is open-backed or closed-back. Because Zerodur® is a ceramic, it must be machined from a single boule, resulting in an open-back architecture. By comparison, ULE® is a glass and can be assembled via frit bonding or low-temperature fusion processes into a closed-back architecture. The advantage

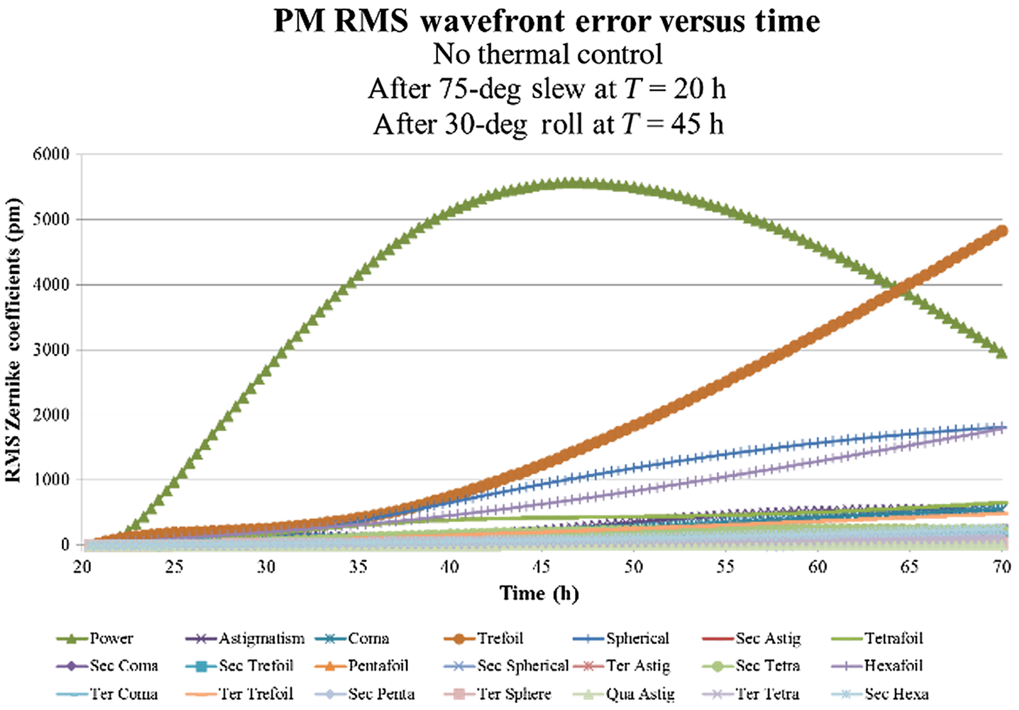

Fig. 24 Changing PM Zernike WFE after 75-deg thermal slew with no thermal control. Power and Trefoil have nanometers of error.

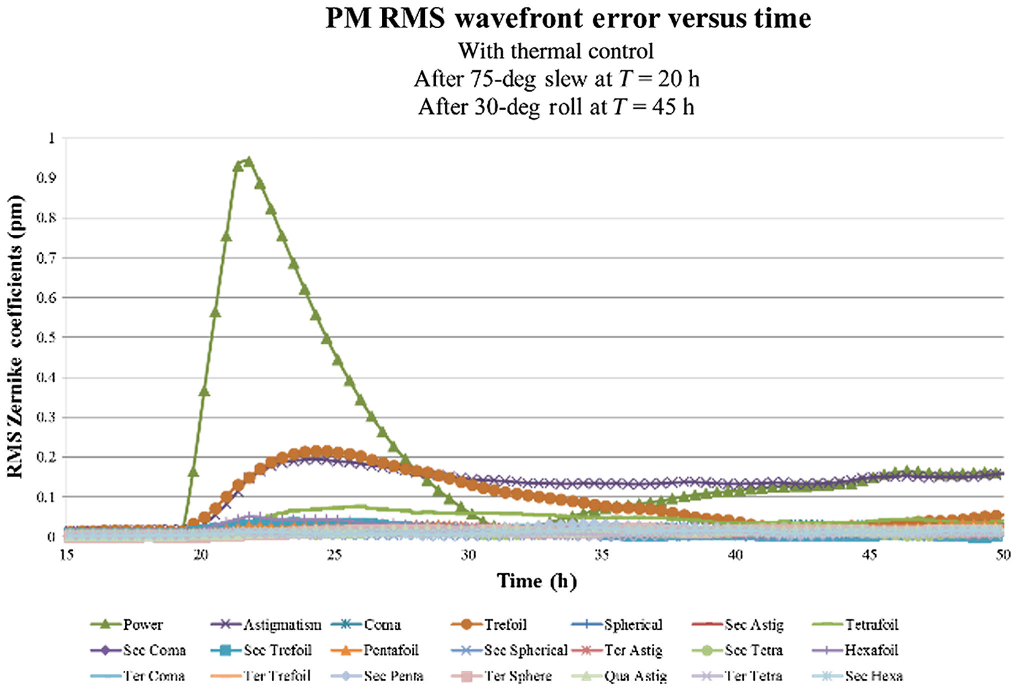

Fig. 25 Changing PM Zernike WFE after 75-deg thermal slew with active zonal thermal control. Power has less than 1 pm increase before being controlled.

is that closed-back mirrors have significantly higher stiffness. Yet, at the same time, because a Zerodur® mirror is machined from a single boule, its CTE distribution can be smoother and more homogeneous. Zerodur® was selected as the baseline material because Schott has demonstrated a routine ability to fabricate 4.2-m-diameter Zerodur® substrates and turn them into lightweight

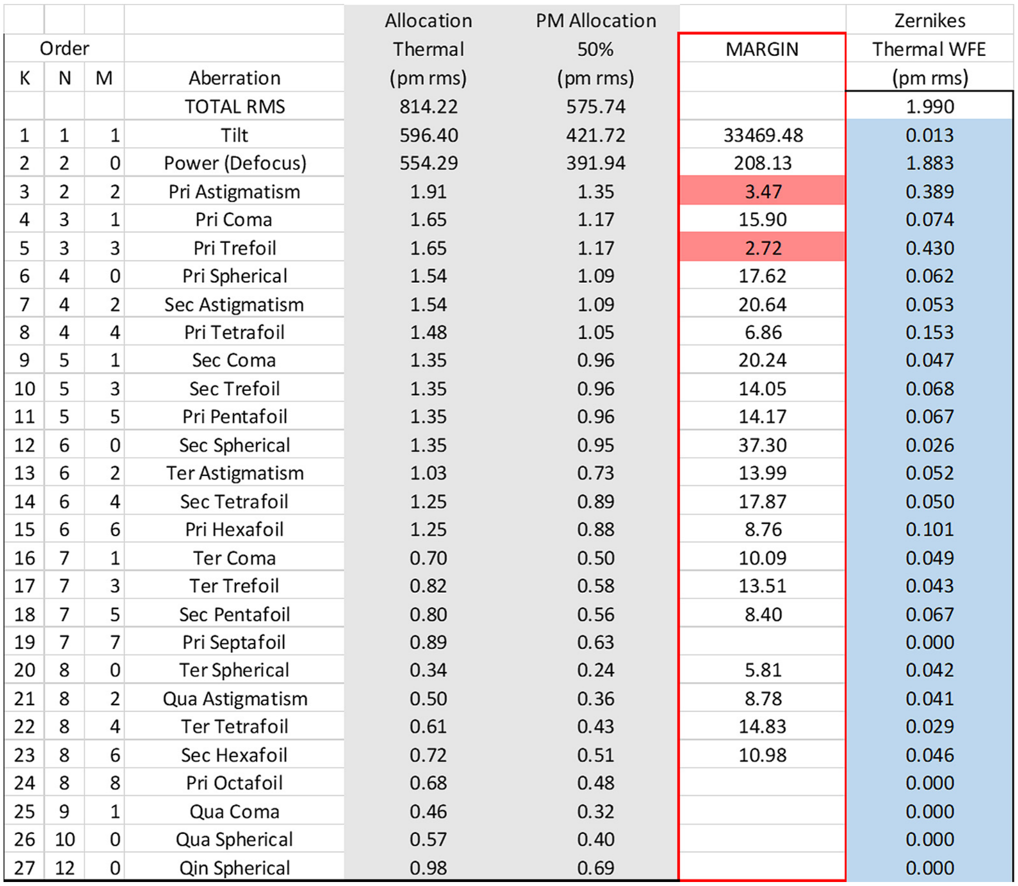

Order K	N	M	Aberration	Allocation Thermal (pm rms)	PM Allocation 50% (pm rms)	MARGIN	Zernikes Thermal WFE (pm rms)
			TOTAL RMS	814.22	575.74		1.990
1	1	1	Tilt	596.40	421.72	33469.48	0.013
2	2	0	Power (Defocus)	554.29	391.94	208.13	1.883
3	2	2	Pri Astigmatism	1.91	1.35	3.47	0.389
4	3	1	Pri Coma	1.65	1.17	15.90	0.074
5	3	3	Pri Trefoil	1.65	1.17	2.72	0.430
6	4	0	Pri Spherical	1.54	1.09	17.62	0.062
7	4	2	Sec Astigmatism	1.54	1.09	20.64	0.053
8	4	4	Pri Tetrafoil	1.48	1.05	6.86	0.153
9	5	1	Sec Coma	1.35	0.96	20.24	0.047
10	5	3	Sec Trefoil	1.35	0.96	14.05	0.068
11	5	5	Pri Pentafoil	1.35	0.96	14.17	0.067
12	6	0	Sec Spherical	1.35	0.95	37.30	0.026
13	6	2	Ter Astigmatism	1.03	0.73	13.99	0.052
14	6	4	Sec Tetrafoil	1.25	0.89	17.87	0.050
15	6	6	Pri Hexafoil	1.25	0.88	8.76	0.101
16	7	1	Ter Coma	0.70	0.50	10.09	0.049
17	7	3	Ter Trefoil	0.82	0.58	13.51	0.043
18	7	5	Sec Pentafoil	0.80	0.56	8.40	0.067
19	7	7	Pri Septafoil	0.89	0.63		0.000
20	8	0	Ter Spherical	0.34	0.24	5.81	0.042
21	8	2	Qua Astigmatism	0.50	0.36	8.78	0.041
22	8	4	Ter Tetrafoil	0.61	0.43	14.83	0.029
23	8	6	Sec Hexafoil	0.72	0.51	10.98	0.046
24	8	8	Pri Octafoil	0.68	0.48		0.000
25	9	1	Qua Coma	0.46	0.32		0.000
26	10	0	Qua Spherical	0.57	0.40		0.000
27	12	0	Qin Spherical	0.98	0.69		0.000

Fig. 26 PM thermal WFE meets its tolerance.

structures via their ELZM machining process. Furthermore, a 1.2-m ELZM owned by Schott and tested at NASA MSFC showed better thermal stability than the 1.5-m ULE® AMTD-2 mirror.[11]

3.3 *Objective 3: Demonstrate Utility of Precision Control Thermal System for Achieving Thermal Stability*

Building a telescope that has an ultra-stable wavefront requires a multi-zone active thermal control system that is beyond the current SOA. Objective 3 demonstrates the ability of advanced thermal control system to control a mirror's shape by determining control variables (heater power levels) based upon state variables (temperature measurements).

3.3.1 *Milestone 3: design, build, and test a multi-zone active thermal control system*

PTC partner L3Harris Corp. designed, fabricated, and delivered a thermal enclosure with 25 zones arranged with cylindrical symmetry—17 zones behind the mirror and six zones on the perimeter (Fig. 27).

The thermal zones were designed to enable correction of thermal gradients, i.e., radial, lateral, and axial (Fig. 28). Radial gradients occur in flight because the mirror views space (at 2.7 K) but is surrounded by structure whose temperature is significantly warmer (270 K). These zones can also be used to compensate for on-orbit errors.

MSFC integrated the enclosure with a thermal sense and control system (Fig. 29). Each zone consisted of heaters capable of operating at 100 V (the maximum voltage before creating concerns of corona discharge in vacuum) and platinum RTD (PT-100) sensors bonded with Stycast® epoxy at the zone's center. The maximum required heater power was determined based upon thermal analysis of the test setup. A data acquisition system with an integral 22-bit digital

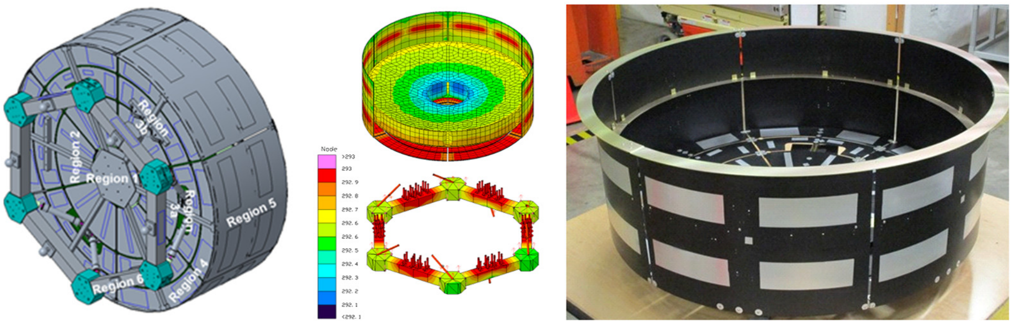

Fig. 27 Thermal control system with 25-zone control for AMTD-2 1.5-m ULE© mirror.

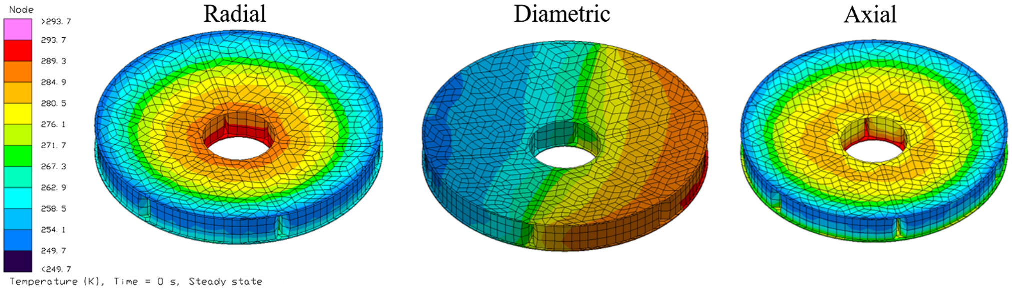

Fig. 28 Thermal control system can introduce radial, lateral, and axial thermal gradients. (All plots have the same vertical scale.)

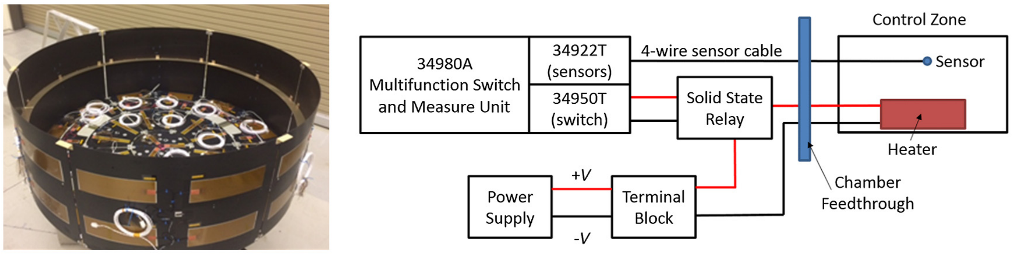

Fig. 29 25-zone thermal enclosure with thermal sensor and control logic diagram.

multimeter was used to measure temperature to the nearest 1 mK. Solid-state relays pulse-width-modulated the power supplied to the heaters to provide proportional power. The controllability achieved by the active thermal control system was limited by the 22-bit 1-mK measurement precision.[26,27]

To demonstrate the capability of active multi-zone thermal control, the system was installed around the 1.5-m AMTD-2 ULE® mirror (Fig. 30) and tested in a relevant environment in the MSFC XRCF (Fig. 31). The XRCF thermal shroud provides a thermal sink for the test and solar lamps impose lateral thermal gradient into the mirror assembly. To minimize thermal load onto the thermal shroud (to keep the refrigeration system stable), insulation was removed from the two control zones nearest to the heat lamps—thus increasing the thermal load into the mirror assembly.[26,27]

The mirror and its mount were fully instrumented with thermal sensors. Pre-test analysis estimated the temperature gradient that would occur during the test. This estimate was used to locate temperature sensors in positions that would provide the best knowledge of the gradients. Figure 32 shows the temperature sensor locations (red dots), heater zones (blue arcs), and the heat lamp array (straight line on right).[27]

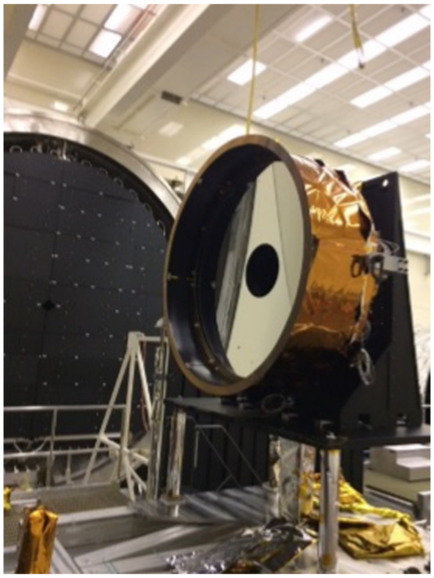

Fig. 30 Thermal system with 1.5-m ULE® mirror.

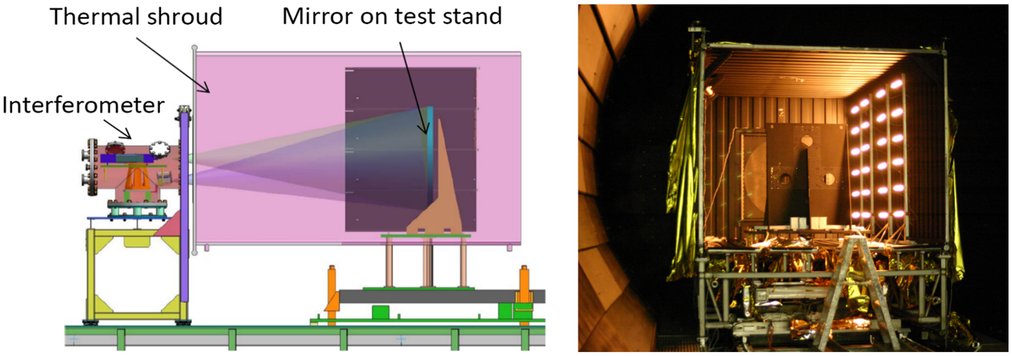

Fig. 31 PTC demonstration XRCF test setup.

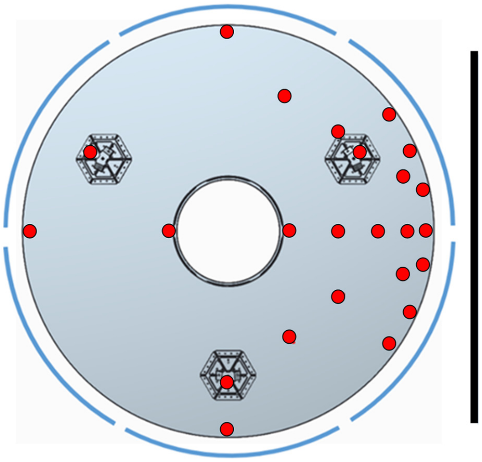

Fig. 32 Locations of thermal sensors (red), control zones (blue), and lamp (black) when viewed from behind the mirror.

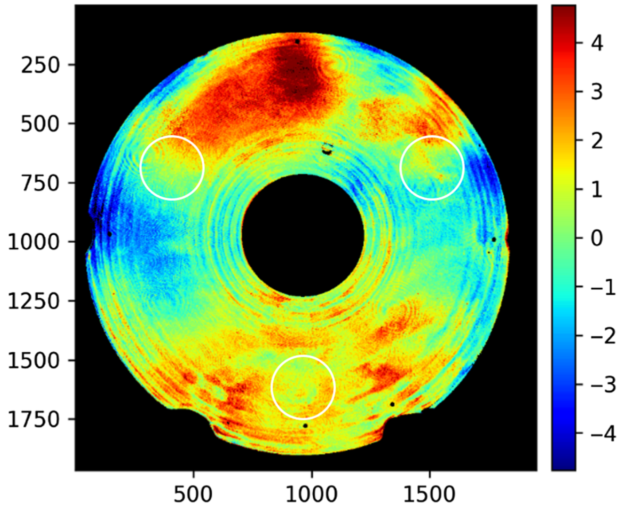

Fig. 33 Repeatability <2-nm rms. Mount locations are circled in white.

As determined by differencing back-to-back averages of 128 phase measurements, the test setup measurement repeatability (uncertainty) was routinely <2-nm rms. (Fig. 33) While cryogen and vacuum pumps introduced vibration, these errors were frozen by the 4D PhaseCam® and eliminated by phase-averaging. The <2-nm rms error was caused by a slow thermal drift of ~1-nm per 6 h and likely indicates CTE inhomogeneity in the mirror.

PTC demonstrated zonal control via three tests. The first demonstrated the ability to eliminate a static radial gradient. The second characterized the ability to compensate for a change in the mirror's thermal environment. The third imposed specific shapes into the 1.5-m ULE® mirror.

Radial gradient elimination test. To produce a radial gradient, the mirror faced a cold wall cooled to 220 K. While the interferometer saw no figure change (because the test setup is blind to power), the multi-zone system's thermal sensors measured a 10-K gradient and eliminated it by adjusting each zone's setpoint temperature. The temperature sensors are orders of magnitude more sensitive to thermal disturbances than the interferometer. Sensor readings over periods of thermal equilibrium had 20-min stability of <2-mK rms.[27] Therefore, in a flight system, once the coronagraph has established a dark hole, perhaps the control system should use thermal sensors to maintain the dark hole.

Thermal environment change test. To characterize the system's response to a dynamic thermal environment, the XRCF was evacuated and thermal shroud cooled to 225 K to cold-bias the test assembly. Once the system achieved thermal equilibrium, heat lamp array next to the PTC thermal system was turned on—first to 360-VA half power (30 VA per lamp) then to full 720-VA power (Fig. 34). At full power, the thermal load on the mirror assembly was equivalent

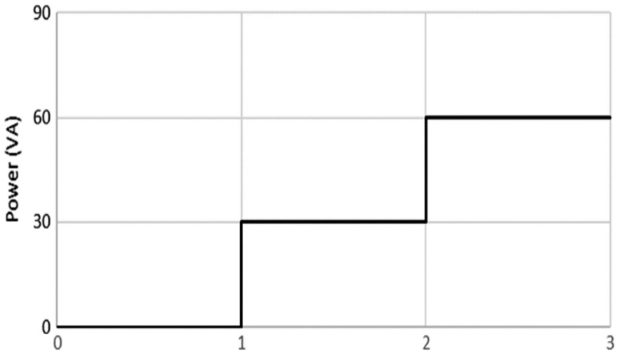

Fig. 34 Solar lamp power.

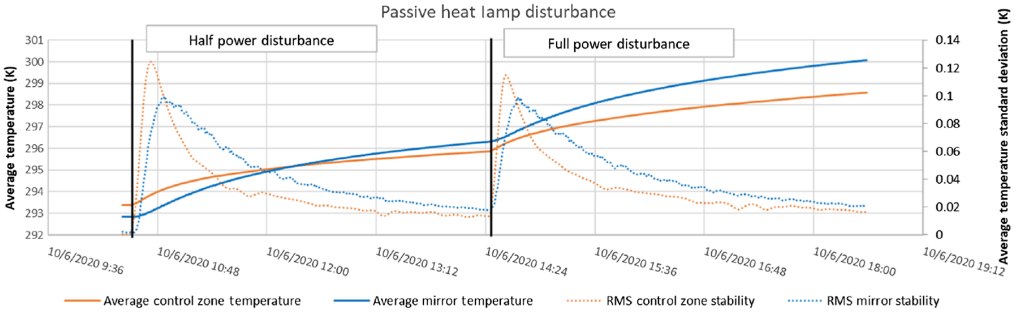

Fig. 35 Mirror response to thermal change without active control. Vertical axis for average temperature is 9.0 K. Vertical axis for stability is 0.14 K.

to increasing the radiant heat load on a baffle by 8000×, increasing baffle temperature of a real space telescope (such as HabEx) from 240 to 400 K. An increase of this magnitude was necessary to overdrive the system sufficient to produce a measurable effect.

The mirror's response to the thermal change was measured twice—first with no control and then with active control. As shown in Fig 35, without control the mirror's maximum thermal instability was ∼100 mK, decaying to ∼20 mK over the 4-h test period. The mirror's average temperature increased ∼7.2 K with a thermal time constant of ∼1 h. The mirror never reached a steady state temperature.[27]

Without active control, the mirror's surface changed by 5-nm rms (Fig. 36). The majority of the change is from the bond pad closest to the thermal load (all bond pads locations are indicated by white circles) and a small amount of astigmatism caused by the lateral thermal gradient. With full power illumination, the mirror had a maximum gradient of 9 K at the end of test (again without reaching steady state). By comparison, the mirror had a nearly 90-K lateral gradient when tested without the thermal enclosure (Fig. 11).

Using active control, the mirror's average temperature increased by <0.25 K with an instability, which, after peaking at ∼20-mK, quickly stabilized to <2 mK (Fig. 37). And, the mirror had a maximum gradient of 1 K at full power, which reached steady state in <1 h.[27] The 0.25-K average temperature increase was caused by a heat leak through the struts and by intentionally leaving insulation off the heater panels closest to the solar lamps (as part of the 8000× overdrive). The initial 20-mK instability is proportional to the 8000× overdriven environment.

In general, an actively controlled mirror's temperature changes and instability have two error sources. The first is control zone. The second is environmental. Control zone error is driven by measurement precision and is attenuated between the control zones and the mirror based upon the mirror's mass and the strength of the radiation conductor between the control system and the

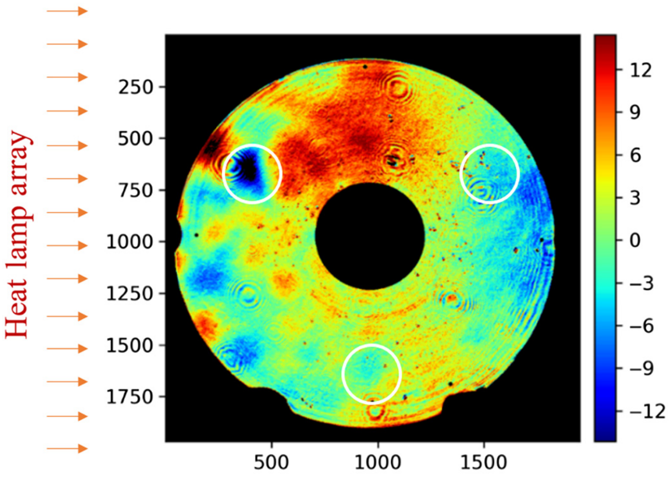

Fig. 36 Mirror response to thermal change with active thermal control. Vertical axis for average temperature is 0.9 K. Vertical axis for stability is 0.14 K.

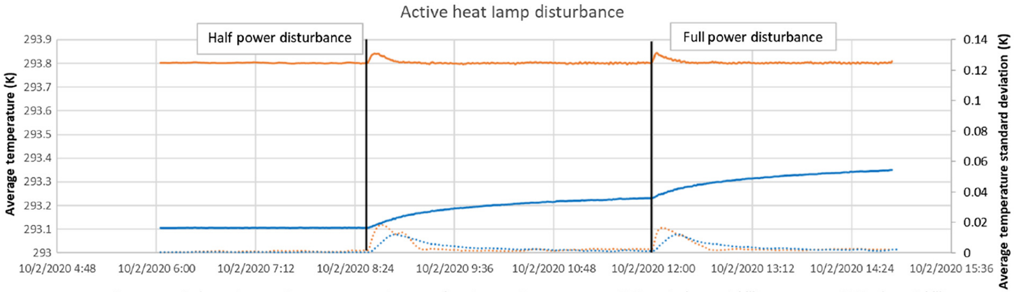

Fig. 37 Mirror response to thermal change with active control.

mirror. Environment errors are driven by thermal load fluctuation, thermal paths that go around the control system, and thermal gradients in the control system.

For the active control test, after the heat lamps are turned up to full power, the mirror's average temperature increases by 0.25 K and stays there, even after the control zones have returned to their set-point temperature, so this temperature change cannot be caused by the control system. Instead, it is proportional to the increase in thermal load. And, because the heat lamp disturbance is ~8000× greater than an on-orbit disturbance and a flight system will have better MLI, the mirror's average on-orbit fluctuation should be <0.03 mK.

The 2-mK steady state stability (in the control zones) is not proportional to the environment, but a limitation of the experiment's 22-bit digitizer which had 1-mK measurement precision. In flight, the mirror would have a stability proportional to the thermal control system stability but attenuated by 100 to 1000× due to weak radiative heat transfer and the mirror's large heat capacitance. So, even with the 2-mK-rms control system stability, a flight mirror would have type 2 error on the order of 0.02-mK rms.[27]

As part of Milestone 2 (Sec. 3.2.1), the thermal stability around a HabEx mirror was defined as a function of the period of the temperature fluctuations (Fig. 14).[7,8] To test the ability of multizonal thermal control to meet this specification, a Fourier transform was performed on test data. Figure 38 plots the performance of the 1.5-m ULE® AMTD-2 (with and without active control) versus the HabEx specification. Please note that while the passive mirror exceeds the HabEx specification, the test has a disturbance that is being overdriven by 8000× greater than if a telescope's baffle changes in temperature by a more flight-like disturbance of 50 mK.

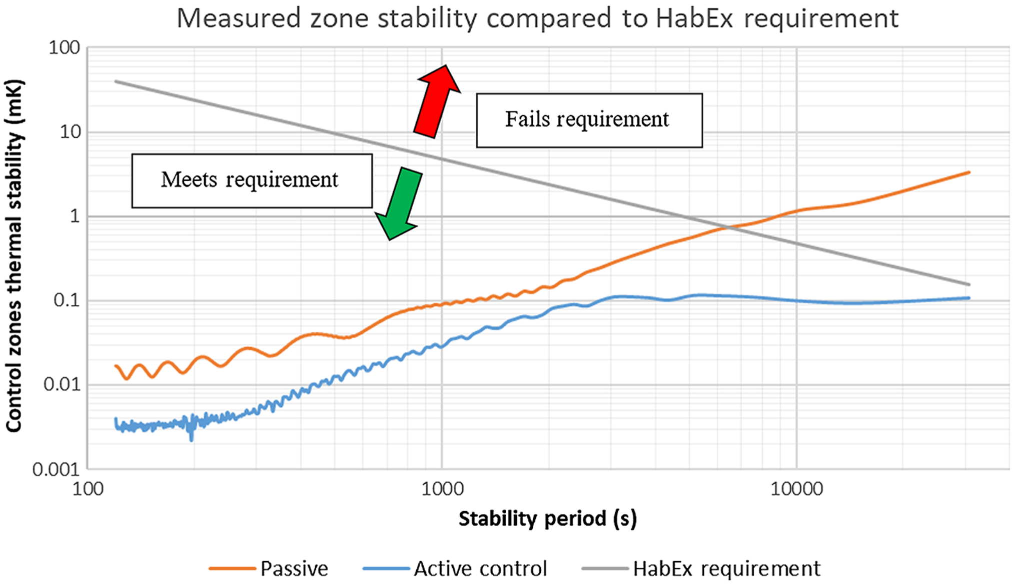

Fig. 38 Measured thermal stability for passive and active heat lamp thermal disturbance test compared to HabEx stability requirement.

Imposed surface figure shape test. The ability of the multi-zone system to impose aberrations was demonstrated by imposing astigmatism, coma, and trefoil shapes into the AMTD-2 mirror. For astigmatism, the surface changed by 16-nm rms as a result of a 30-K thermal gradient. For coma, the surface change was 6.8-nm rms for a 34-K gradient. And, for trefoil, a 25-K thermal gradient produced a 7-nm rms shape change. Figures 39–44 show (a) control zone temperatures and (b) imposed astigmatic, coma, and trefoil surface figures shapes, respectively. Figures 42–44 are movies of these shapes being imposed onto the mirror's surface.

This ability to shape the mirror using temperature enables another way to correct common low-order aberrations that might arise on orbit. Also, it gives an indication of the sensitivity of the mirror to thermal instability. If the mirror's thermal distribution can be controlled with a

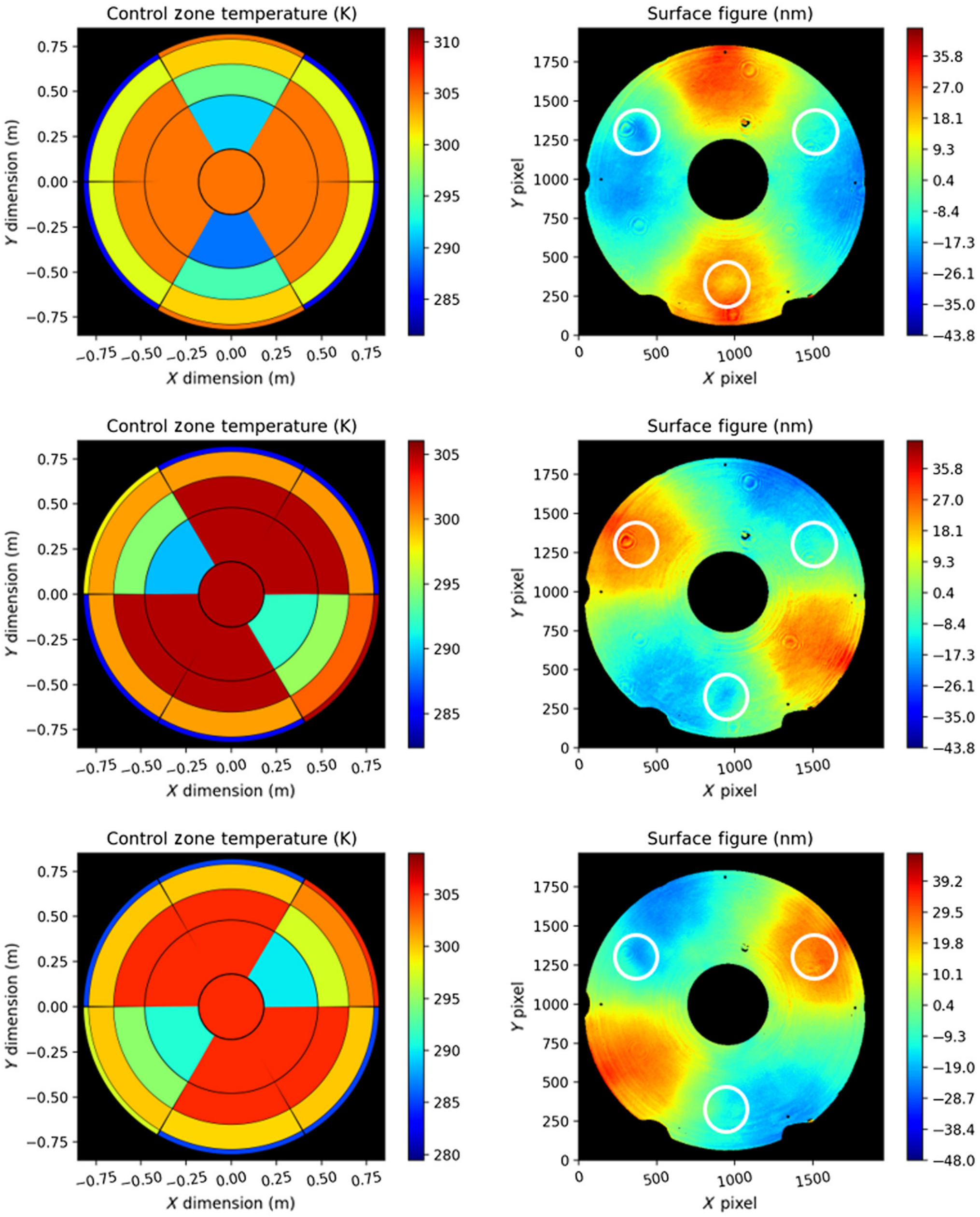

(a) (b)

Fig. 39 (a) Control zone temperatures and (b) imposed astigmatic surface figure shape.

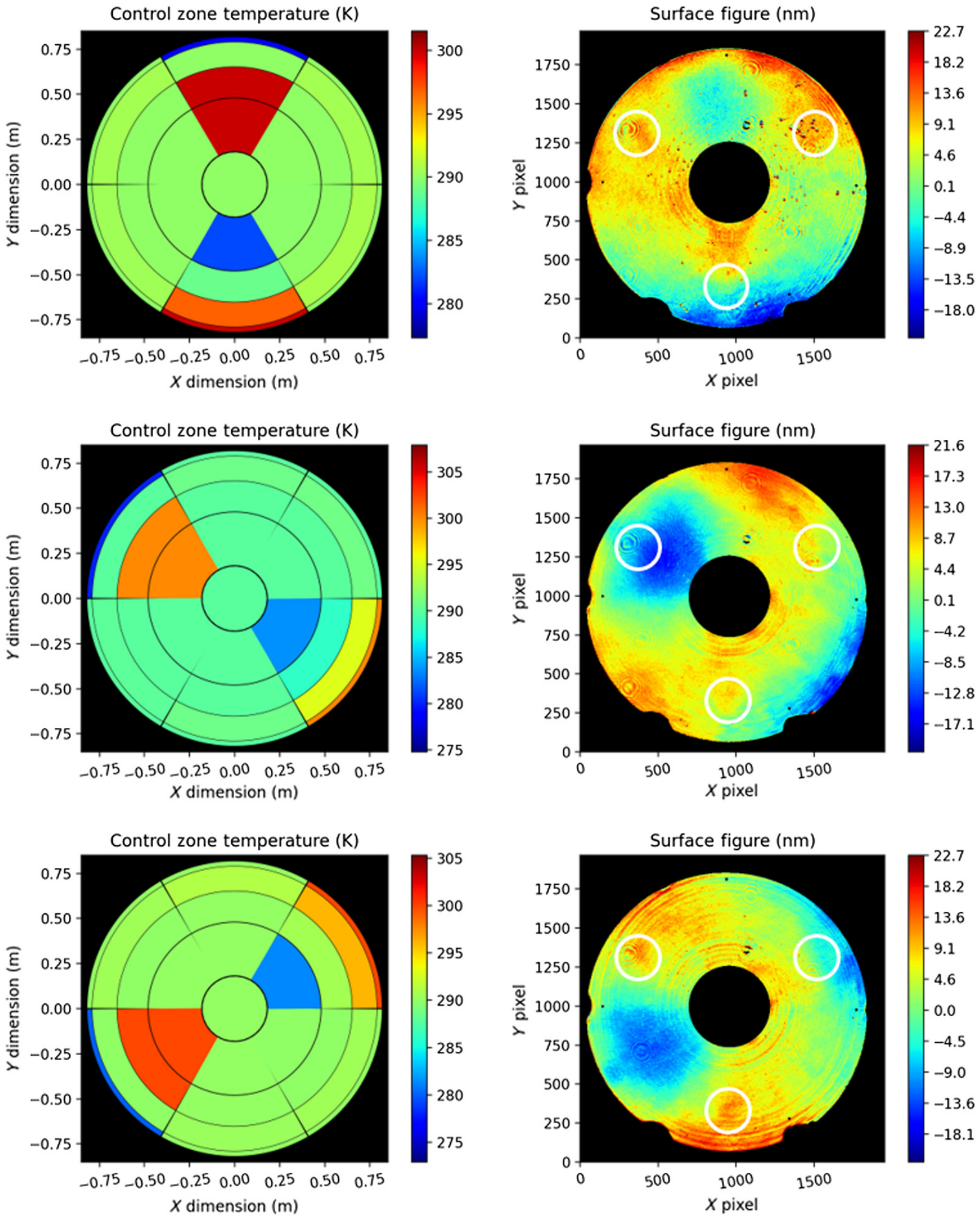

(a) (b)

Fig. 40 (a) Control zone temperatures and (b) imposed coma surface figure shape.

stability of 2 mK, then its shape should be stable at the picometer level, i.e., the stability required to enable coronagraphy. The measured thermal correctability are given in Table 1.

4 Mid-Spatial Frequency Error Stability

While not an original PTC objective, our data enabled an analysis approach for quantifying thermally induced mid-spatial frequency error which can cause speckle noise in the coronagraph dark hole. General astrophysics and exoplanet science drive the PM's spatial frequency specification. General astrophysics is most sensitive to the shape and stability of the point spread function (PSF), which is driven by low-spatial frequency errors. And, exoplanet science is most sensitive to mid- and high-spatial frequency errors. Mid-spatial frequency errors blur or spread

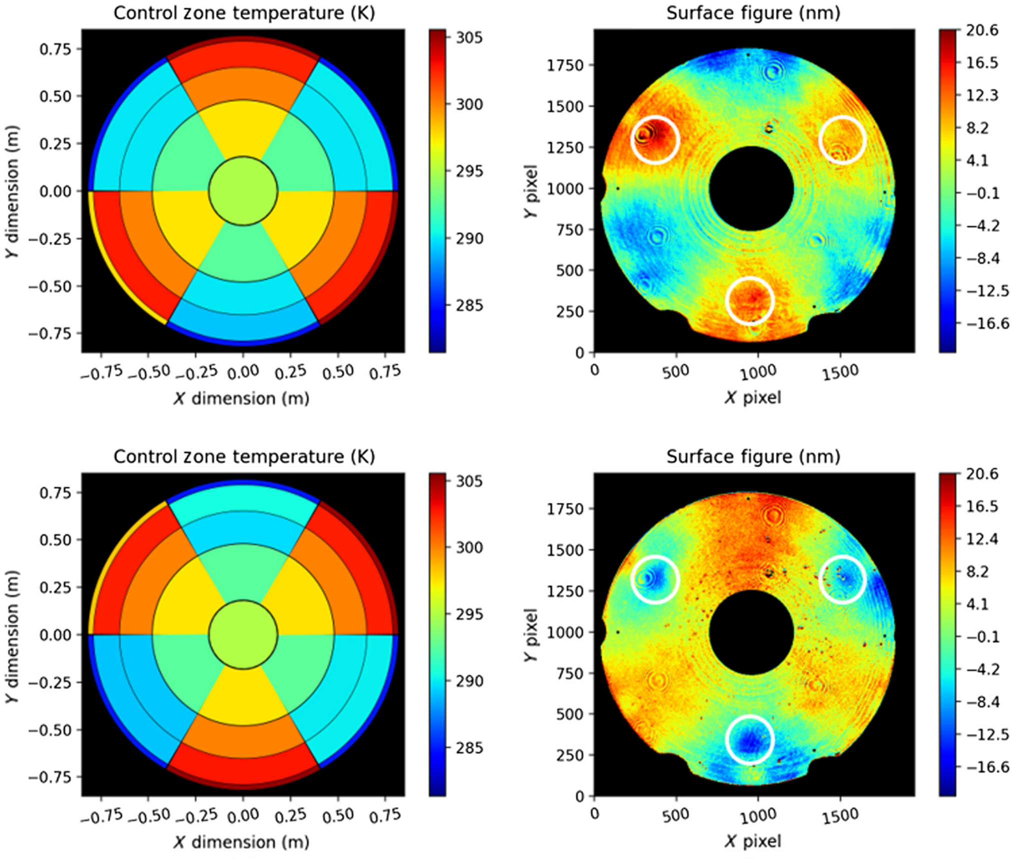

(a) (b)

Fig. 41 (a) Control zone temperatures and (b) imposed trefoil surface figure shape.

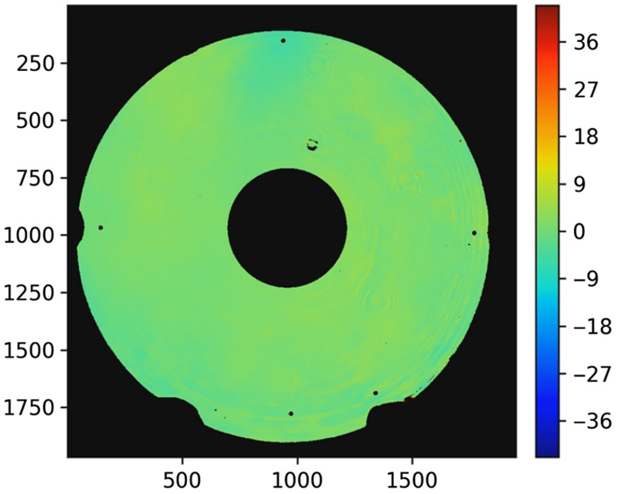

Fig. 42 Video 1 showing imposed astigmatic surface figure shape (Video 1, MOV, 2.6 MB [URL: https://doi.org/10.1117/1.JATIS.8.2.024001.1]).

the core. And high-spatial frequency errors and surface roughness scatter light out of the core and over the entire PSF. Thus, per Table 2, the HabEx total PM surface figure specification is divided into low-, mid-, and high-spatial frequency bands.

This specification assumes computer-controlled polishing for spatial frequencies to 30 cycles (50-mm minimum tool size) to correct quilting error and a −2.5 power spectral density (PSD)

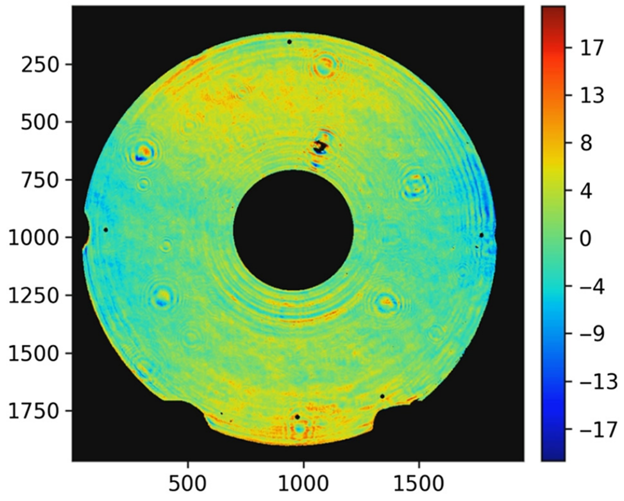

Fig. 43 Video 2 showing imposed coma surface figure shape (Video 2, MOV, 4.6 MB https://doi.org/10.1117/1.JATIS.8.2.024001.2]).

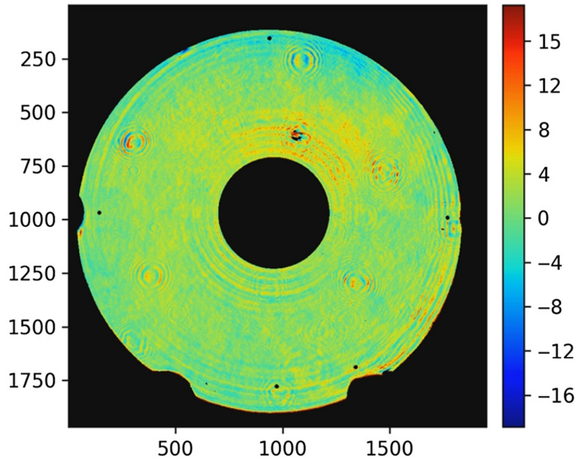

Fig. 44 Video 3 showing imposed trefoil surface figure shape (Video 3, MOV, 4 MB https://doi.org/10.1117/1.JATIS.8.2.024001.3]).

Table 1 Measured thermal correctability.[27]

Surface shape	PV correctability (nm/K)	RMS correctability (nm/K)
Astigmatism	1.3	0.53
Coma	0.6	0.20
Trefoil	0.8	0.28

slope for high spatial frequencies. The 100-cycle boundary between mid- and high-spatial error is defined assuming that the coronagraph uses a 64×64 deformable mirror (DM). A 64×64 DM can theoretically correct spatial frequencies up to 32 cycles (or half the number of DM elements). This could create a dark hole with an inner working angle (IWA) of λ/D and an outer working angle of $32\lambda/D$. The system engineering consideration is that PM spatial frequency errors up to 3× beyond what can be corrected by the DM can scatter energy back into

Table 2 PM error specification.

Total surface error	<5.6 nm rms (nm rms)
Low-spatial SFE (<30 cycles/dia)	<4.3
Mid-spatial SFE (30 to 100 cycles)	<3.3
High-spatial SFE (>100 cycles)	<1.4
Roughness	<0.3

Table 3 Cryo-deformation SFE per K.

	AMTD 1.5-m ULE® Mirror (pm/K rms)	Schott 1.2-m Zerodur® Mirror (pm/K rms)
Total surface error	465	153
Low-spatial SFE (<30 cycles/dia)	305	50
Mid-spatial SFE (30 to 100 cycles)	45	31
High-spatial SFE (>100 cycles)	40	36

the dark hole. Therefore, the PM needs have a surface figure as smooth as possible (better than 4-nm rms) for spatial frequency errors from 30 cycles up to 100 cycles.[28,29]

But as discussed in Sec. 3.2.1 and shown in Fig. 16, beyond having nanometer precision—to prevent speckle noise that reduces contrast in the dark hole—the telescope WFE needs to be stable at the picometer level for spatial frequencies from 1.5 cycles per diameter to 100 cycles per diameter. Table 3 gives the band-limited-rms SFE of the 1.5-m AMTD ULE® mirror's cryo-deformation (Fig. 9) and the 1.2-m Schott Zerodur® mirror's cryo-deformation (Fig. 18); and Figs. 45 and 46 show the PSD of these two mirrors.

Finally, Table 4 and Fig. 47 give the residual mid-spatial WFE produced by imposing each of the low-order surface figure shapes shown in Figs. 39–41. The created residual error was calculated by subtracting the uniform temperature state of the mirror from the maximum thermal gradient that produced each surface shape. Then, the first 36-Zernike terms were removed from each difference. The residual PSD of these imposed shapes is consistent with the cryo-deformation PSD for the 1.5-m ULE® mirror.

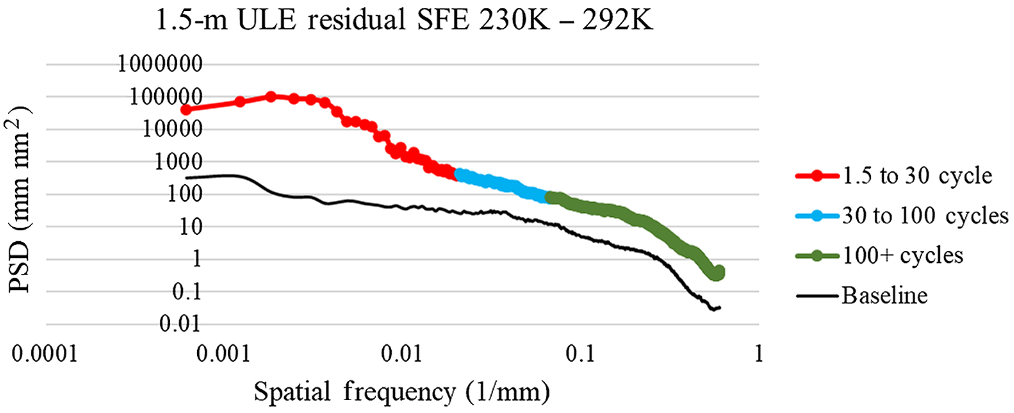

Fig. 45 PSD of AMTD 1.5-m ULE® mirror cryo-deformation error after removing first 36-Zernike terms. Black baseline is measurement repeatability.

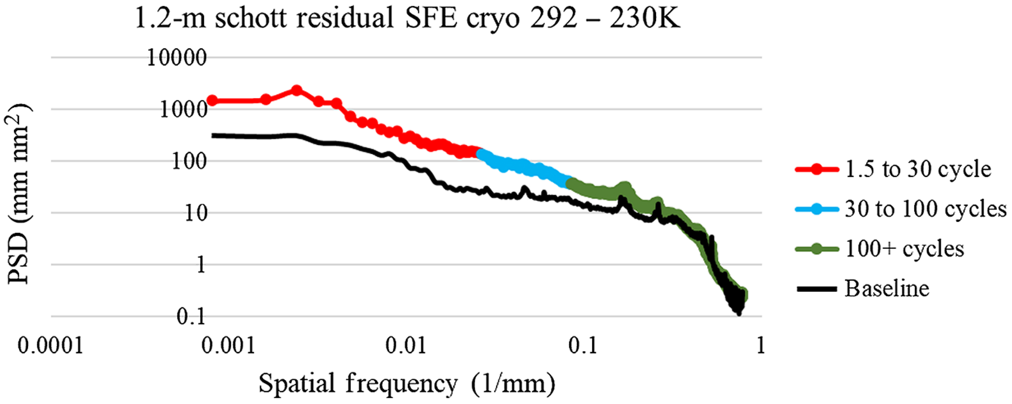

Fig. 46 PSD of Schott 1.2-m Zerodur® mirror cryo-deformation error after removing first 36-Zernike terms. Black baseline is measurement repeatability.

Table 4 Residual SFE RMS per nm PV of imposed shape change.

	Astigmatism (pm-rms/nm-PV)	Coma (pm-rms/nm-PV)	Trefoil
Total surface error	140	133	118
Low-spatial SFE (<30 cycles/dia)	92	73	63
Mid-spatial SFE (30 to 100 cycles)	45	66	59
High-spatial SFE (>100 cycles)	63	78	55

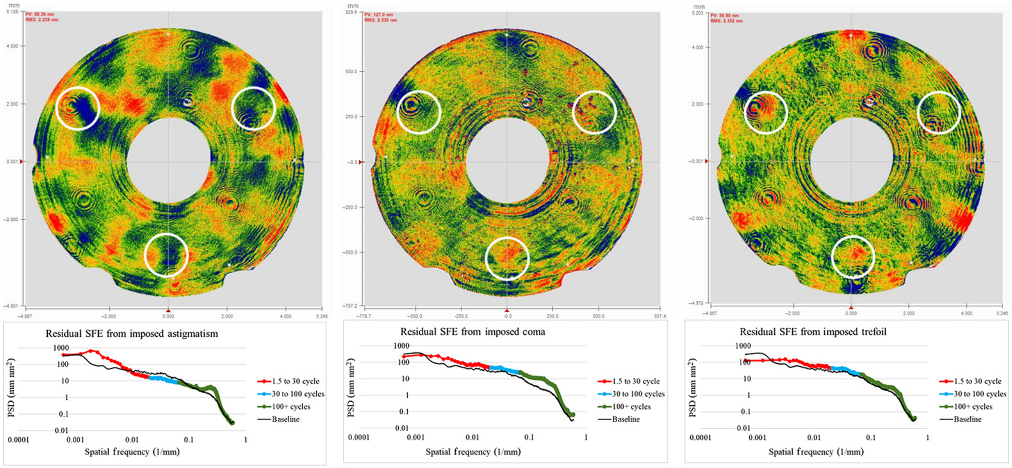

Astigmatism Coma Trefoil

Fig. 47 Residual surface error and PSD of AMTD-2 mirror imposed shape change after removing first 36-Zernike terms. PSD shows residual mid-spatial frequency error relative to measurement noise threshold.

5 Conclusion

The PTC project was a multiyear effort initiated in fiscal year 2017 to mature the TRL of technologies required to enable ultra-thermally stable ultraviolet/optical/infrared space telescope primary-mirror assemblies for ultra-high-contrast observations of exoplanets. PTC successfully completed its three objectives: (1) validate thermal optical performance models, (2) derive thermal system stability specifications, and (3) demonstrate multi-zonal active thermal control.

PTC assessed that it has advanced the maturity of multi-zonal active thermal control to at least TRL-5 using a 25-zone active thermal system to control the response of the 1.5-m AMTD-2 ULE® mirror to thermal stimuli in a relevant environment. PTC's key accomplishments are a demonstration of better than 2-mK-rms stable thermal control of the 1.5-m ULE© AMTD-2 mirror when exposed to an 8000× over-driven thermal disturbance in a relevant thermal/vacuum environment, the ability to shape the 1.5-m ULE® mirror to picometer precision, and an analysis approach for quantifying thermally induced mid-spatial frequency error which can cause speckle noise in the coronagraph dark hole. Finally, critical to achieving thermal stability is having a primary mirror with sufficient thermal mass that its thermal time constant is significantly (many orders of magnitude) longer than its control system period.

Acknowledgments

PTC is funded by a NASA Science Mission Directorate (SMD) Astrophysics Division (APD) Internal Science Funding Model (ISFM) Directed Work Package. Others contributing to the work summarized in this paper include (in alphabetical order) from NASA MSFC: Stephany Andrews, William Arnold, Pat Bagley, Mark Baker, Ron Beshears, Stephen Cheney, Chris Crutcher, Michael R. Effinger, Ron Eng, Randy Goode, Charlie Griffith, Harlan Haight, Thomas Hill, Bill Hogue, Steve Johnson, Jeff Kegley, Tomasz Lis, Jennie Mccall, Shelia Nash-Stevenson, Darron Rice, Harry Rutledge, Richard Siler, W. Scott Smith, Chet Speegle, Mark Stahl, Paul Tatum, Ernie Wright and Roy Young; ESSCA: Jim Duffy, Art Lapietra, Terry Lee, Scott Marona, Zakkary McPeters, Amy Meekham, Carl Widrig, John Tucker, and Mark Young; Logical Innovations, Inc.: Melissa Harkins and Micah Moore-Wilridge; AI Systems: William Arnold; University of Alabama Huntsville: Bijan Nemati, and Leah Sheldon; NASA Pathways Interns: Meghan Carrico, Adam Cedrone and Tim Little; and from Harris Corporation: Jesse Cramer, Robert Day, Robert Egerman, Scott Gade, Keith Havey, Carl Rosati, and Piero Terio.

References

1. Committee for a Decadal Survey of Astronomy and Astrophysics and National Research Council, *New Worlds, New Horizons in Astronomy and Astrophysics*, The National Academies Press, Washington, D.C. (2010).
2. Cosmic Origins Program Office and NASA, "Cosmic origins program annual technology report," 2015, https://cor.gsfc.nasa.gov/docs/2015CORPATRRev1.pdf.
3. "JWST technical report 13-JWST0207 F," NASA (2013).
4. M. D. Lallo, "Experience with the Hubble Space Telescope: 20 years of an archetype," *Opt. Eng.* **51**, 011011 (2012).
5. J. E. Krist et al., "End-to-end coronagraphic modeling including a low-order wavefront sensor," *Proc. SPIE* **8422**, 844253 (2012).
6. K. Havey, Private Communication, Harris Corporation (2019).
7. T. Brooks, H. P. Stahl, and W. R. Arnold, "Advanced Mirror Technology Development (AMTD) thermal trade studies," *Proc. SPIE* **9577**, 957703 (2015).
8. T. E. Brooks, "Predictive thermal control applied to HabEx," *Proc. SPIE* **10398**, 1039814 (2017).
9. A. R. Barron, "Universal approximation bounds for superpositions of a sigmoidal function," *IEEE Trans. Inf. Theory* **39**, 930–945 (1993).
10. T. E. Brooks, "Computed tomography and stiction in a low temperature slumped mirror," Mirror Technology Days in the Government (2017).
11. T. E. Brooks, R. Eng, and H. P. Stahl, "Optothermal stability of large ULE and Zerodur mirrors," *Proc. SPIE* **10743**, 107430A (2018).
12. H. P. Stahl and T. E. Brooks, "Predictive thermal control (PTC) technology to enable thermally stable telescopes: first two-year status," *Proc. SPIE* **11116**, 111160U (2019).
13. H. P. Stahl, "Advanced ultraviolet, optical, and infrared mirror technology development for very large space telescopes," *J. Astron. Telesc. Instrum. Syst.* **6**(2), 025001 (2020).

14. R. Eng, "Cryogenic optical and mechanical test result of a 1.5-meter lightweighted ULE mirror assembly (Conference Presentation)," *Proc. SPIE* **10742**, 1074202 (2018).
15. M. J. Edwards, "Today's ULE® material of choice for premier optics," Mirror Technology Days in the Government (2018).
16. H. P. Stahl, M. Postman, and W. S. Smith, "Engineering specifications for large aperture UVO space telescopes derived from science requirements," *Proc. SPIE* **8860**, 886006 (2013).
17. M. T. Stahl, H. P. Stahl, and S. B. Shaklan, "Preliminary analysis of effect of random segment errors on coronagraph performance," *Proc. SPIE* **9605**, 96050P (2015).
18. S. Gaudi et al., "The habitable exoplanet observatory (HabEx) mission concept study final report," 2020, https://www.jpl.nasa.gov/habex/pdf/HabEx-Final-Report-Public-Release-LINKED-0924.pdf.
19. H. P. Stahl et al., "Habitable-zone exoplanet observatory (HabEx) baseline 4-m telescope design and predicted performance," *Proc. SPIE* **11115**, 111150U (2019).
20. H. P. Stahl et al., "Habitable-zone exoplanet observatory baseline 4-m telescope: systems-engineering design process and predicted structural thermal optical performance," *J. Astron. Telesc. Instrum. Syst.* **6**(3), 034004 (2020).
21. B. Nemati et al., "HabEx telescope WFE stability specification derived from coronagraph starlight leakage," *Proc. SPIE* **10743**, 107430G (2018).
22. B. Nemati et al., "Method for deriving optical telescope performance specifications for Earth-detecting coronagraphs," *J. Astron. Telesc. Instrum. Syst.* **6**(3), 039002 (2020).
23. T. E. Brooks et al., "Modeling the extremely lightweight zerodur mirror (ELZM) thermal soak test," *Proc. SPIE* **10374**, 103740E (2017).
24. W. R. Arnold and H. P. Stahl, "Design trade Study for a 4-meter off-axis primary mirror substrate and mount for the Habitable-zone Exoplanet direct imaging mission," *Proc. SPIE* **10398**, 1039808 (2017).
25. T. Westerhoff et al., "Lightweighted ZERODUR for telescopes," *Proc. SPIE* **9151**, 91510R (2014).
26. H. P. Stahl et al., "Predictive thermal control (PTC) technology to enable thermally stable telescopes: year four status," *Proc. SPIE* **11820**, 118200A (2021).
27. T. E. Brooks and T. P. Stahl, "Extreme dimensional stability thermal control test," *Proc. SPIE* **11819**, 118190B (2021).
28. S. B. Shaklan, J. J. Green, and D.M. Palacios, "The Terrestrial Planet Finder Coronagraph optical surface requirements," *Proc. SPIE* **6265**, 62651I (2006).
29. S. B. Shaklan and J. J. Green, "Reflectivity and optical surface height requirements in a coronagraph," *Appl. Opt.* **45**, 5143 (2006).

Thomas E. Brooks is an aerospace engineer at MSFC Advanced Concepts Office. He was co-investigator on Predictive Thermal Control. He has a background in numerical modeling focusing on in thermal and structural analysis, and has analyzed, designed, and tested flight systems on International Space Station and in Low Earth Orbit as well as a payload scheduled to launch to the moon in 2022. He received his MS degree in aerospace systems engineering from the University of Alabama in Huntsville in 2014.

H. Philip Stahl is a senior optical physicist at NASA MSFC and a leading authority in optical systems engineering and metrology. He matures technology for large space telescopes; was responsible for Webb Telescope mirrors; and developed Stahl telescope cost model. He is fellow of SPIE and OSA, past ICO vice president, and SPIE 2014 president. He received his BA degree in physics and mathematics from Wittenberg University 1979, and his MS and PhD degrees in optical science from the University of Arizona in 1983 and 1985, respectively.